Impact of Desert Dust Radiative Forcing on Sahel Precipitation: Relative Importance of Dust Compared to Sea Surface Temperature Variations, Vegetation Changes, and Greenhouse Gas Warming

MASARU YOSHIOKA AND NATALIE M. MAHOWALD

Donald Bren School of Environmental Science and Management, and Institute of Computational Earth System Science, University of California, Santa Barbara, Santa Barbara, California, and Climate and Global Dynamics Division, National Center for Atmospheric Research, Boulder, Colorado*

ANDREW J. CONLEY AND WILLIAM D. COLLINS

Climate and Global Dynamics Division, National Center for Atmospheric Research, Boulder, Colorado*

DAVID W. FILLMORE

Climate and Global Dynamics Division, National Center for Atmospheric Research, and Program in Atmospheric and Oceanic Sciences, University of Colorado, Boulder, Colorado*

CHARLES S. ZENDER

Department of Earth System Science, University of California, Irvine, Irvine, California

DANI B. COLEMAN

Climate and Global Dynamics Division, National Center for Atmospheric Research, Boulder, Colorado*

(Manuscript received 26 January 2006, in final form 3 July 2006)

ABSTRACT

The role of direct radiative forcing of desert dust aerosol in the change from wet to dry climate observed in the African Sahel region in the last half of the twentieth century is investigated using simulations with an atmospheric general circulation model. The model simulations are conducted either forced by the observed sea surface temperature (SST) or coupled with the interactive SST using the Slab Ocean Model (SOM). The simulation model uses dust that is less absorbing in the solar wavelengths and has larger particle sizes than other simulation studies. As a result, simulations show less shortwave absorption within the atmosphere and larger longwave radiative forcing by dust. Simulations using SOM show reduced precipitation over the intertropical convergence zone (ITCZ) including the Sahel region and increased precipitation south of the ITCZ when dust radiative forcing is included. In SST-forced simulations, on the other hand, significant precipitation changes are restricted to over North Africa. These changes are considered to be due to the cooling of global tropical oceans as well as the cooling of the troposphere over North Africa in response to dust radiative forcing. The model simulation of dust cannot capture the magnitude of the observed increase of desert dust when allowing dust to respond to changes in simulated climate, even including changes in vegetation, similar to previous studies. If the model is forced to capture observed changes in desert dust, the direct radiative forcing by the increase of North African dust can explain up to 30% of the observed precipitation reduction in the Sahel between wet and dry periods. A large part of this effect comes through atmospheric forcing of dust, and dust forcing on the Atlantic Ocean SST appears to have a smaller impact. The changes in the North and South Atlantic SSTs may account for up to 50% of the Sahel precipitation reduction. Vegetation loss in the Sahel region may explain about 10% of the observed drying, but this effect is statistically insignificant because of the small number of years in the simulation. Greenhouse gas warming

* The National Center for Atmospheric Research is sponsored by the National Science Foundation.

Corresponding author address: Masaru Yoshioka, School of Geographical Sciences, University of Bristol, University Road, Bristol, BS8 1SS, United Kingdom.
E-mail: m.yoshioka@bristol.ac.uk

DOI: 10.1175/JCLI4056.1

seems to have an impact to increase Sahel precipitation that is opposite to the observed change. Although the estimated values of impacts are likely to be model dependent, analyses suggest the importance of direct radiative forcing of dust and feedbacks in modulating Sahel precipitation.

1. Introduction

The rainfall decrease and devastating droughts in the Sahel region during the last three decades of the twentieth century are among the largest recent climate changes recognized by the climate research community (e.g., Dai et al. 2004). The large temporal and spatial coherence of the dry (and wet) conditions are the exceptional characteristics of rainfall variability in the Sahel (Nicholson and Grist 2001). A number of studies have investigated the possible causes or mechanisms of the Sahelian drought in the last 30 yr. In general, the studies examine either land–atmosphere interactions or forcing from sea surface temperatures (SSTs). The land–atmosphere investigators include Xue and Shukla (1993), Xue (1997), Clark et al. (2001), Taylor et al. (2002), and Xue et al. (2004), and they demonstrate that land surface degradation leads to reduced precipitation in North Africa using numerical simulations. The forcing studies by Folland et al. (1986), Lamb and Peppler (1992), Rowell et al. (1995), Bader and Latif (2003), Giannini et al. (2003), and Hoerling et al. (2006) show that large-scale sea surface temperature patterns are closely related to precipitation patterns over North Africa. Many of these studies have identified the role of the interhemispheric SST contrast (i.e., SST difference between Northern and Southern Hemispheres) in the Atlantic basin as the most important mechanism, and the dry condition in Sahel is associated with lower North and higher South Atlantic SSTs compared to the climatological mean. Xue and Shukla (1998), Zeng et al. (1999), and Wang et al. (2004) argue that both the land–atmosphere interaction and SST control are required to reproduce the magnitude and duration of observed precipitation variability.

On the other hand, some authors such as Nicholson (2000) and Prospero and Lamb (2003) hypothesize that dust may play a role in the changes in Sahel climate. They note that dust radiative forcing is significant in this region and can modulate the interhemispheric SST gradient that may be responsible to the precipitation variability in the Sahel. Dust can also provide a mechanism necessary for the interannual coherence since dust entrainment into the atmosphere is limited by vegetation, which is correlated with precipitation in the previous year (e.g., Prospero and Lamb 2003). Miller and Tegen (1998) and Miller et al. (2004, hereafter MTP04) have examined the climatic effects of dust using general circulation model (GCM) simulations and found precipitation reductions over the tropical North Atlantic and adjacent continental areas including the Sahel and Guinea Coast regions. They emphasize the importance of surface radiative forcing in modulating hydrologic cycles.

This study investigates the possible effects of direct radiative forcing of dust on Sahel precipitation through its impacts on the atmosphere and the surface. We also characterize relative roles of dust and other processes such as SSTs, vegetation change, and greenhouse gas (GHG) warming using simulations with an atmospheric general circulation model. This study represents the first time that the relative importance of dust forcing and other mechanisms for the changing Sahel precipitation are examined in the same modeling framework. The next section describes the model we use and the experimental designs we have performed. Section 3 presents the radiative forcing of dust simulated in the model and compares it with previous studies. Section 4 summarizes the responses of precipitation and SSTs to dust radiative forcing at the global scale. Section 5 investigates the Sahel precipitation responses to SSTs, vegetation change, greenhouse gas warming, and dust radiative forcing, and evaluates their relative roles. Section 6 summarizes our findings and concludes the study.

2. Methods

The National Center for Atmospheric Research's (NCAR's) Community Climate System Model version 3 (CCSM3) is a coupled atmosphere, land, ocean, and sea ice model (Collins et al. 2006a). This model is used for simulating past, present, and future climate changes, such as for Houghton et al. (2001). Here we describe the mineral aerosol and surface vegetation changes incorporated in the Community Land Model version 3 (CLM3; Dickinson et al. 2006) and Community Atmosphere Model version 3 (CAM3; Collins et al. 2006b) to examine the effects of dust, sea surface temperature, vegetation change, and greenhouse gases.

a. Dust modeling

The dust model used in this study is described in more detail in Mahowald et al. (2006), including detailed comparisons of the model simulations of dust to available observations. The model resolution is about

2.8° horizontally near the equator (T42) and 26 levels vertically. The dust source mechanism follows the Dust Entrainment and Deposition Module (Zender et al. 2003a) and work conducted in the offline Model of Atmospheric Transport and Chemistry (MATCH; Mahowald et al. 2002, 2003; Luo et al. 2003; Mahowald and Luo 2003). The sources of dust are assumed to be dry, unvegetated regions subject to strong winds. The magnitude of the dust source is calculated within the CLM3. In the default version of the model, the satellite vegetation climatology of vegetation is the same as that used for other land surface calculations in the model (Bonan et al. 2002). Sensitivity studies using modified vegetation data are described below. When the total leaf area index plus the stem area index is below 0.1, the area of the grid box available for dust generation is assumed to increase linearly with decreasing vegetation cover (Mahowald et al. 2006).

The source scheme parameterizing dust entrainment into the atmosphere is described in detail in Zender et al. (2003a). The model calculates a wind friction threshold velocity based on the surface roughness and soil moisture, and dust is entrained into the atmosphere when the friction velocity exceeds this threshold. The model assumes that the optimum size distribution of soil particles is available for saltation and subsequent vertical flux (~75 μm). However, after the dust flux is calculated, the dust source magnitude is multiplied by a soil erodibility factor to include the impact of differences in soil size and texture following the "preferential source" concept (Ginoux et al. 2001). We use the geomorphic soil erodibility factor described by Zender et al. (2003b). A wind friction threshold is calculated following Iversen and White (1982). This threshold is modified for two different processes in the model. Following Fecan et al. (1999), the threshold wind friction velocity increases with increasing soil moisture. The fetch of the winds over this erodible surface is allowed to modify the wind friction velocity threshold as well (Gillette and Passi 1988). Once the wind friction threshold velocity is calculated, the horizontal saltation fluxes are calculated (White 1979); vertical fluxes are a small fraction of the horizontal flux (Marticorena and Bergametti 1995). In this scheme, the effects of subgrid-scale variation of wind in dust emission and drying of top soil (affecting threshold velocity) by strong wind will not be simulated.

We use four aerosol size bins with boundaries at 0.1, 1.0, 2.5, 5.0, and 10.0 μm in diameter. The transported aerosols are assumed to have a subbin distribution based on a lognormal distribution just like Zender et al. (2003a; see Fig. 1) although we use a mass median diameter (MMD) of 3.5 μm as reported by Reid et al. (2003), which is larger than the value used in Zender et al. (2003a; 2.5 μm). Hand et al. (2004) have shown the model using MMD of 2.5 μm underestimates fine and overestimates coarse particles (Hand et al. 2004, p. 16), and Arimoto et al. (2006) recently reported even larger MMD of 5.5 μm for the long-range transported Asian dust. Mass fractions at source in the four bins are 3.8%, 11%, 17%, and 67% as predicted in Grini and Zender (2004) using the saltation–sandblasting model. This size distribution tends toward larger particles than many previous studies (e.g., Tegen and Fung 1994; Ginoux et al. 2001; Mahowald et al. 2002; Zender et al. 2003a; Luo et al. 2003; MTP04).

Deposition processes include dry gravitational settling, turbulent dry deposition, and wet deposition during precipitation events. Both dry depositional processes are modeled using parameterizations described in Zender et al. (2003a), with a mass flux advection scheme in order to parameterize vertical fall rates correctly (Rasch et al. 2001; Ginoux 2003). Wet depositional processes are parameterized within the CAM3 similar to Rasch et al. (2001). The dust determined using the processes described above is referred to as the prognostic dust (prescribed dust is described below).

Shortwave radiative effects are calculated within CAM3 every hour. A delta-Eddington approximation is adopted for the shortwave using 19 discrete intervals (Collins 1998) for each vertical layer in the model (Collins et al. 2004). Longwave effects are calculated every 12 h in CAM3, which uses an absorptivity/emissitivity formulation for longwave heating (Ramanathan and Downey 1986). A broadband approach with seven bands is used, which accounts for the water vapor window regions (Collins et al. 2002). The indices of refraction have been derived from Patterson (1981) for the visible wavelengths, Sokolik et al. (1993) for the near infrared, and Volz (1973) for the infrared. The imaginary part of indices of refraction in the visible wavelength were scaled to match the new estimates of Sinyuk et al. (2003) and Dubovik et al. (2002) for the region 0.33 to 0.67 μm. These estimates are based on satellite- and surface-based field observations and may still be susceptible to biases due to measurement errors and contaminations. Scattering of longwave radiation by dust is neglected in radiative calculations. This may lead to underestimates of longwave radiative forcing by up to 50% at top of the atmosphere (TOA) and 15% at the surface (SFC; Dufresne et al. 2002).

b. Vegetation change

We do not include the Dynamic Global Vegetation Model (DGVM) version of the CLM3 because when coupled to the CAM3, it produces unrealistically large

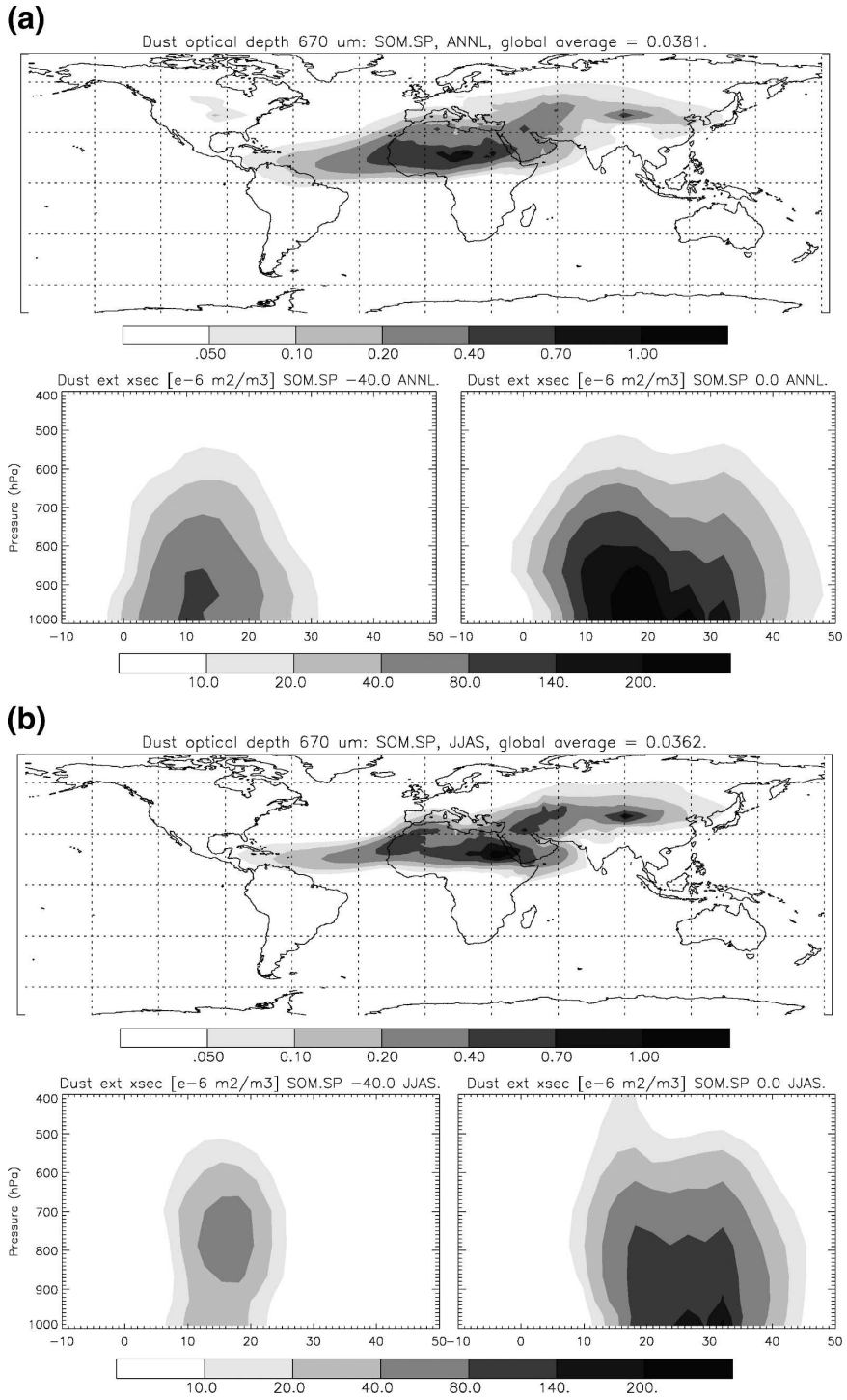

FIG. 1. (a) Annual (top) mean optical depth and meridional cross sections of extinction cross section at (bottom left) 40°W and (bottom right) at the prime meridian of prognostic dust at 670 nm (case SOM.SP). (b) Same as in (a), but for the Sahel rainy season (JJAS).

dust plumes (not shown) due to dry biases in both CAM3 and CLM3 (Collins et al. 2006a; Dickinson et al. 2006). However, vegetation dynamics is thought to have a strong control on precipitation and dust emissions. Vegetation itself is controlled by precipitation during previous months and years. For example, the observed increase of dust in the Atlantic since the 1970s may be partly due to vegetation loss near the Sahara

TABLE 1. List of simulations.

AMIP: CAM3 coupled with CLM3 and forced by historical SST.	
AMIP.ND	No dust radiative forcing: 1951–93.
AMIP.NDV	Same as AMIP.ND, but with wet-period vegetation: 1951–70.
AMIP.S	Dust SW radiative forcing and feedback: 1951–93.
AMIP.SL	Dust SW and LW radiative forcing and feedback: 1951–93.
AMIP.SLV	Same as AMIP.SL, but with wet-period vegetation in 1951–70 combined with AMIP.SL with normal vegetation in 1971–93.
AMIP.SLVH	Same as AMIP.SLV, but dust in the wet period is reduced by half.
AMIP.F	Forced by historical SST only. All other forcings are fixed at 1990s levels. Climatological dust is prescribed and prognostic dust is not calculated: 1951–2000; five ensemble members.
AMIP.H	Forced by historical SST, GHG, aerosols, and solar forcings. Climatological dust is prescribed and prognostic dust is not calculated: 1951–2000; five ensemble members.
SOM: CAM3 coupled with CLM3 and coupled with the Slab Ocean Model.	
SOM.ND	No dust radiative forcing: 30 yr.
SOM.S	Dust SW radiative forcing and feedback: 30 yr.
SOM.SL	Dust SW and LW radiative forcing and feedback: 30 yr.
SOM.SLV	Same as SOM.SL, but with wet-period vegetation: 30 yr.
SOM.SP	Dust SW radiative forcing to and response of prescribed monthly mean annually cyclic dust just as the default version of CAM. Prognostic dust is calculated but it does not affect the simulation in any way. Used to derive dust radiative forcings: 30 yr.
SOM.SP2	Same as SOM.SP, but with doubled CO_2. Used to estimate the effects of increased greenhouse gasses: 9 yr.

desert boundary that has been inhibiting dust emission, and this vegetation change is considered to be a result of the well-known drought in the sub-Saharan transition zone called the Sahel (Prospero and Nees 1986; Tegen and Fung 1995; Mahowald et al. 2002; Prospero and Lamb 2003). To evaluate the role of vegetation change in the Sahel on precipitation through changing surface heat and moisture fluxes and surface albedo as well as through changing dust sources, Sahelian vegetation in the predrought (or wet) period (1950s through mid-1960s) is deduced using observed rainfall record and estimated intensity of cultivation in that period as explained below. The dry period is represented as the default vegetation in the model, since the CLM3 uses vegetation from the 1990s. This is the only variation in the vegetation considered in this study. The simulation using doubled CO_2 uses the same dry period vegetation in order to isolate the effect of CO_2 although in the real world a higher level of CO_2 has a significant impact on the vegetation.

Tucker and Nicholson (1999) argue that annually averaged precipitation in the Sahel has a constant gradient and is relatively zonally uniform. They also show that changes in the location of the southern boundary of the Sahara Desert correlate with interannual rainfall anomalies. Using a linear regression model fitted to the latitudes of the Saharan boundary and rainfall anomalies given in Tucker and Nicholson (1999; $R^2 = 0.82$) and using decadal rainfall change from Nicholson (1995), we estimate that the desert boundaries have been shifted about 2° southward during the dry period relative to the wet period. We have constructed the distribution of natural vegetation in the wet period in the transition zone by shifting the default natural vegetation in CLM (derived from observation in 1992) between 10° and 20°N northward by 2° while expanding the vegetation between 8° and 10°N into the band between 8° and 12°N with reducing the gradient by a half. If we use the rainfall data of Dai et al. (2004), we get a smaller vegetation shift of 1.4 degrees but the variance explained by the linear model is lower ($R^2 = 0.58$).

The fraction of cultivated land in 1950s–60s is estimated based on two scenarios. Ramankutty and Foley (1999) have obtained an increasing intensification of agriculture but found little increase in the area of croplands (25%) from 1950s–60s to 1992 in the Sahel (data are available at http://www.sage.wisc.edu/). On the other hand, extrapolating the model simulation of Stephenne and Lambin (2001) in Burkina Faso, we estimate an almost fourfold increase in the area of cropland in the Sahel. Despite the large difference, however, vegetation cover based on these two scenarios produces little change in dust emissions in our model simulations (not shown). We chose to use the Sahelian wet-period vegetation incorporating cultivated land based on Ramankutty and Foley (1999) for the simulations in this study.

c. Simulations

The cases of simulations are listed in Table 1. The GCM simulations are conducted either forced by observed SSTs or coupled with a Slab Ocean Model

(SOM; Collins et al. 2006b). The configuration forced by observed SSTs is called the Atmospheric Model Intercomparison Project (AMIP) case below since this is the model configuration used for the Atmospheric Model Intercomparison Project (Gates 1992). When SOM is coupled to CAM3, it simulates SST changes in response to dust radiative effects and atmospheric changes, although changes in ocean circulations are not included in an SOM simulation. In its default configuration, CAM3 includes the radiative effects of externally given (i.e., prescribed) aerosol climatology in the calculation of radiative fluxes and heating rates in the shortwave but not in the longwave (Collins et al. 2006b). The climatology has been derived from a chemical transport model constrained by assimilation of satellite retrievals of aerosol optical depth (Collins et al. 2001; Rasch et al. 2001). The SOM.SP and AMIP.SP cases use the default shortwave radiative forcing of the prescribed dust. Although it calculates prognostic dust, prognostic dust has no effect on the atmosphere and the surface. The default aerosol forcing is also used in the SOM.SP2 case to estimate the effects of doubled CO_2 concentration in this study.

Radiative forcing is obtained by conducting one year of simulation in the SOM.SP case where at each time step the calculations of radiative fluxes and atmospheric heating are repeated for three conditions: the default radiative effects (shortwave forcing of the prescribed dust), no dust radiative effects, and shortwave and longwave radiative effects of prognostic dust calculated using the instantaneous dust distribution from the dust source, transport, and deposition schemes described above. Radiative forcing is calculated as the difference in radiative flux or heating rate calculated with radiative effects of prognostic dust and that with no dust radiative effects. The values calculated with the default radiative effects are passed to the next time step to continue the simulation. Because this computation is expensive we only conduct this calculation for one year, similar to previous studies (e.g., Miller et al. 2006).

This study analyzes simulations with radiative effects and feedback of prognostic dust. Both AMIP and SOM simulations are conducted with no dust radiative effect (ND), dust shortwave forcing and feedback (S), and dust shortwave and longwave forcing and feedback (SL). Simulations with shortwave and longwave forcing and feedback are also performed using the vegetation cover in the wet period described in the previous section (SLV). Additionally, AMIP simulations are also conducted with wet-period vegetation without radiative forcing (NDV) and with radiative forcing of a half of the simulated strength of dust. In addition, five member ensembles of the AMIP.F and AMIP.H simulations are also analyzed. AMIP.F simulations use the default model configurations and are forced by the historical SST field only while all other external forcings are interannually invariant. AMIP.H is similar to the AMIP.F but also includes time-varying forcing by volcanoes, greenhouse gases, aerosols, and solar variability. In these cases, climatological monthly dust is prescribed as in the SOM.SP case but prognostic dust is not calculated. All AMIP and SOM simulations except AMIP.H and SOM.SP2 use external forcings fixed at the levels of 1990 except SSTs.

All SOM simulations are conducted for 31 yr, and all but the first year of the simulations are used for analyses because global average temperature reached the equilibrium after the first year. AMIP cases are simulated from 1950 to 1993 or longer, and the period between 1951 and 1993 is used for analyses. The exceptions are the AMIP.NDV, AMIP.SLV, and AMIP.SLVH simulations, which are performed for only 1950–70, and the latter two are combined with AMIP.SL after this. These simulations thus use the wet-period vegetation for the appropriate time period.

d. Statistical significances and uncertainties of the estimates

The statistical significance of differences between two groups of data values is quantified using the Student's *t* test using a significance level of 99% in sections 3 and 4. However in section 5, we estimate precipitation changes due to different processes, where each of the steps involves uncertainty and these uncertainties propagate through the calculations. To evaluate the statistical significance of the final estimates, we use confidence intervals. The confidence interval of a mean is defined as mean plus and minus 1.96 times the standard error. Here, 1.96 is the 97.5 percentile value of the standard normal distribution and hence gives a probability of 0.95 in a two-tailed test. The standard error of a mean is given as standard deviation divided by square root of the sample size (Anderson and Finn 1996).

Standard errors for derived quantities, such as difference between two groups of data and product or ratio of two variables with uncertainties, are calculated using the propagation of errors. Based on the formulas for standard deviation (e.g., Bevington 1988), formulas for standard errors can be derived; $\delta_y^2 = \delta_1^2 + \delta_2^2 \pm 2r\delta_1\delta_2$ for $y = x_1 \pm x_2$, and $(\delta_y/\bar{y})^2 = (\delta_1/\bar{x}_1)^2 + (\delta_2/\bar{x}_2)^2 \pm 2r(\delta_1/\bar{x}_1)(\delta_2/\bar{x}_2)$, plus for $y = x_1x_2$ and minus for $y = x_1/x_2$, where $\bar{x}_1$, $\bar{x}_2$, and $\bar{y}$ are the means and δ_1, δ_2, and δ_y are the standard errors of x_1, x_2, and y, respectively, and r is correlation coefficient between x_1 and x_2. The last term diminishes when two datasets (x_1 and x_2) are independent. For example, the last term needs to be

included to evaluate the uncertainty in the difference in annual precipitation between two AMIP simulations, both of which are forced by the same SST and hence considered correlated to each other, while it can be neglected for difference of SOM simulations. A value estimated using multiple sets of data is considered statistically significant at a 95% level if the estimate is larger than the confidence interval (i.e., standard error times 1.96) determined using this method.

3. Dust distribution and radiative forcing

Mahowald et al. (2006) show that the model is able to capture the observed annually averaged optical depth and deposition patterns well. Figures 1a,b show annual and Sahel rainy season [June–September (JJAS)] averages, respectively, of optical depth and extinction cross section at 670 nm at West Africa and Central Atlantic for prognostic dust simulated in the SOM.SP case. Annual mean dust optical depth (DOD) is up to 30% higher in the AMIP.SL and SOM.SL simulations and 5% lower in the AMIP.SLV and SOM.SLV simulations over regions of heavy dust loading including North Africa and the tropical North Atlantic than the case shown in Fig. 1a. The annual average dust optical depth is high over the Sahel region (10°–20°N over Africa) in general and it maximizes over the central to eastern Sahel. Dust optical depth tends to be high over the northern Sahel in summer (Fig. 1b) and the southern portion in winter (not shown). It also tends to be high over eastern North Africa in summer compared to other seasons (Fig. 1b). Optical depth of North African dust is highest in spring and lowest in fall (not shown). A large part of dust loading is in the lower to middle troposphere, but in summer over the Atlantic dust loading maximizes between 900 and 600 hPa, which corresponds to the Saharan air layer (SAL) mentioned in the literature (e.g., Carlson and Prospero 1972; Karyampudi et al. 1999).

Figure 2 shows shortwave (Fig. 2a), longwave (Fig. 2b), and net (shortwave + longwave; Fig. 2c) radiative forcings at the TOA, in the atmosphere (ATM), and at the SFC in the SOM.SP case. Figure 2a represents radiative forcings similar to those in the AMIP.S and SOM.S cases whereas Fig. 2c represents those similar to those in the AMIP.SL and SOM.SL cases. Table 2 summarizes the forcings averaged over the globe, the North Atlantic (0°–30°N, 50°–20°W), and North Africa (5°–35°N, 18°W–40°E). These show that the shortwave effects of dust are reduced downward fluxes at TOA and SFC and enhanced absorption within ATM, and the longwave effects are the opposite. The relative magnitude of shortwave and longwave effects are different over land and ocean. At the surface and within the atmosphere, the shortwave forcing dominates over the ocean, but the longwave forcing is comparable to or even larger than the shortwave forcing over land. There are several reasons for this. The TOA and SFC shortwave forcings are larger over ocean than over land (especially bright surfaces like desert) because dust has higher albedo than the ocean surface and reflects more light back into space (Coakley and Chylek 1975). The ATM shortwave absorption is more effective over land because solar radiation reflected at the bright surface has more chance to be absorbed by dust (Coakley and Chylek 1975). There are several reasons that the longwave forcing is more effective over desert. The hotter desert surface emits more longwave radiation. The longwave radiation interacts more efficiently with larger particles, while the shortwave radiation interacts more efficiently with smaller particles. Since larger particles have shorter lifetimes and can travel shorter distances, the longwave forcing is larger near dust source regions while the shortwave forcing has smaller gradients. Also, the vapor path between the surface and dust is small over deserts. This allows the relatively cold dust to interact with the longwave radiation from the surface and results in reduced outgoing and increased downwelling longwave radiation. As a result, the shortwave forcing is greater than the longwave forcing over the North Atlantic, but shortwave and longwave forcings have similar magnitudes over North Africa.

Table 2 also compares our simulation results in dust radiative forcing with existing calculations and simulations. Globally, our shortwave forcing is more negative at TOA and smaller within the atmosphere than Woodward (2001) and MTP04, while it is comparable at the surface. Also, our longwave forcing is much larger than in these studies, and so our model even has opposite signs of net forcing over the Sahara from their simulations (see figures in their studies). These differences in the shortwave can be explained by our higher single-scattering albedo (i.e., less absorbing), which is due to our smaller imaginary part of the indices of refraction in the shortwave range following Sinyuk et al. (2003). As a result, our single-scattering albedo is several percent (~7% at 495 nm) higher than MTP04. Our larger longwave forcing can be explained by our larger particle sizes. Our dust model has about 4 times as much silt (>1 μm) and about 1/3 of clay particles (<1 μm) compared to MTP04, in order to compare better with new observations (Reid et al. 2003). Also, as mentioned earlier, smaller particles interact with shortwave radiation more effectively than larger particles do, and larger particles do exactly the opposite. There may also be effects of differences in surface albedo and vertical dis-

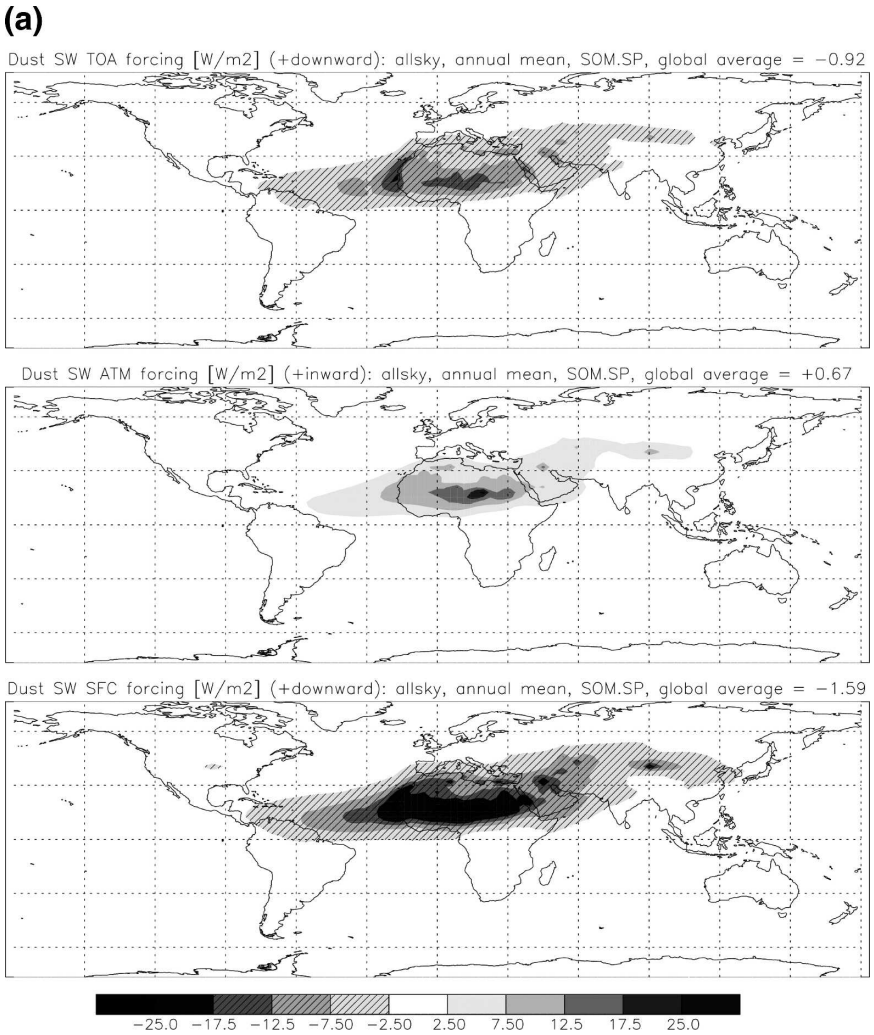

FIG. 2. (a) Annual mean shortwave radiative forcing by prognostic dust (case SOM.SP). [(top), (bottom) Net fluxes (positive downward) at the top of the atmosphere and the surface. (middle) Atmospheric absorption (W m^{-2}).] (b) Same as in (a), but for longwave radiative forcing. (c) Same as in (a), but for net (shortwave + longwave) radiative forcing.

tribution of dust. Our surface albedo averaged over the Sahara is 0.27 while the value in MTP04 is 0.33 (R. L. Miller 2004, personal communication).

In a more recent study, Miller et al. (2006) have revised dust optical properties to be similar to those used in this study, based on the updated refractive indices obtained from Sinyuk et al. (2003). In global average, their particle size distribution is similar to but a little on the larger side compared to ours. They have also increased their longwave radiative forcing by 30% to account for the effect of longwave scattering, which our radiative calculations do not include. Their results (also shown in Table 2) are much closer to ours compared to the studies considered above, although our longwave forcing is still stronger even without longwave scattering. We hypothesize that the differences in longwave between this model and Miller et al. (2006) are due to the differences in the radiative transfer models as well as simulated vertical distribution of dust and interactions with other factors such as clouds and water vapor, but testing the relative importance of these mechanisms is beyond the scope of this study.

Carlson and Benjamin (1980) show calculations of Saharan radiative forcing over ocean surface with no cloud condition using two methods: their own method (first numbers) and the more detailed Wiscombe model. The discrepancies are large at a small optical depth although they agree well at larger optical depths. The differences between their results and ours are again consistent with the difference in the aerosol

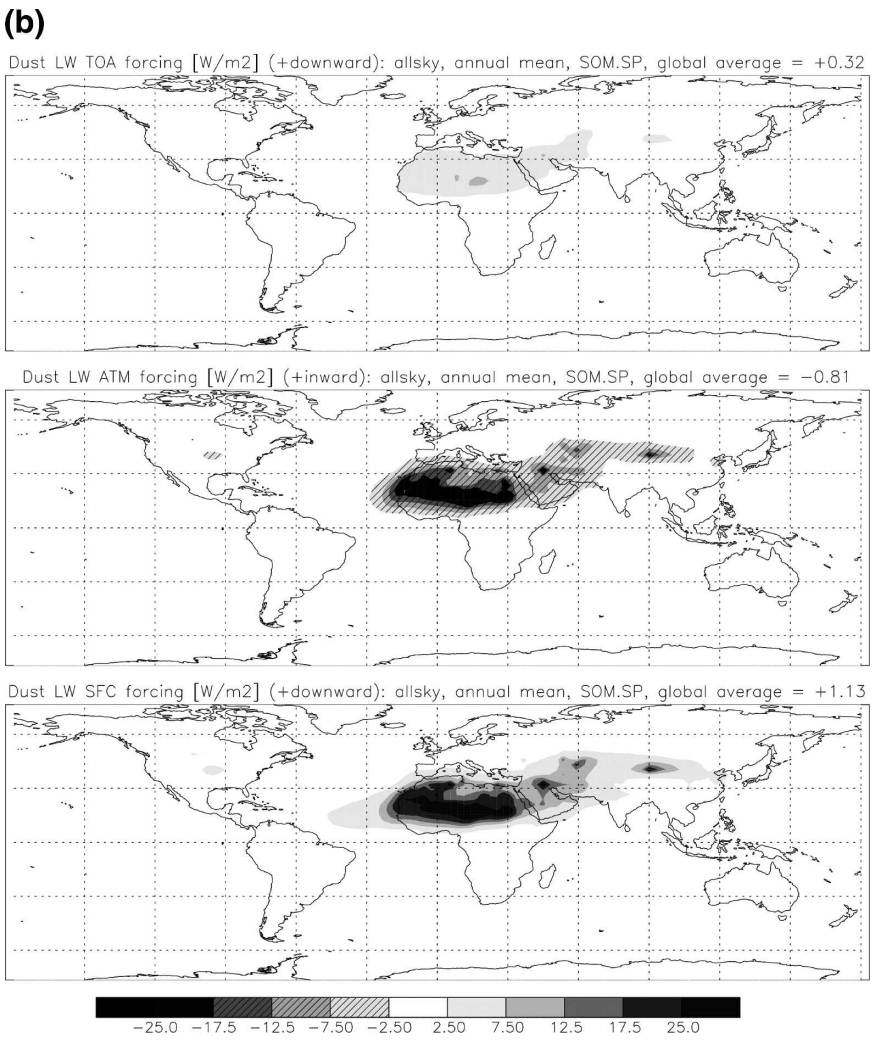

FIG. 2. (*Continued*)

model; their dust has lower single-scattering albedo and more large particles than ours.

Comparisons show that our results are more similar to available observations. Li et al. (2004) report diurnal mean shortwave forcing efficiency of –32∼–38 W m^{-2} per unit optical depth at 550 nm in June–August (JJA) and –23∼–29 W m^{-2} per unit optical depth in November–January (NDJ) based on satellite observation of Saharan dust over the Atlantic Ocean. Our TOA shortwave forcing efficiencies averaged over the North Atlantic (0°–30°N, 50°–20°W) of –24.8 W m^{-2} per unit optical depth (–3.0 W m^{-2} for DOD = 0.12) in JJA and –29.8 W m^{-2} per unit optical depth (–6.3 W m^{-2} for 0.21) in NDJ are approximately in this range.

Zhang and Christopher (2003) report a TOA longwave forcing efficiency of +11∼+20 (area average of +15) W m^{-2} per unit optical depth of dust over the Sahara in September in satellite measurements in cloud-free conditions. Haywood et al. (2005) show a similar range of TOA longwave forcing efficiency for surface temperatures between 300 and 320 K from theoretical calculations. We obtain cloud-free longwave forcing efficiencies averaged over the Sahara (20°–30°N, 10°W–30°E) of +19.1 W m^{-2} per unit optical depth in July (+9.3 W m^{-2} for DOD = 0.49) and +16.7 W m^{-2} per unit optical depth in September (+7.0 W m^{-2} for DOD = 0.42).

Therefore, our shortwave and longwave radiative forcing calculations are quite reasonable in terms of comparisons with observations. The differences with other studies are within the uncertainties of the observations since dust size distributions and optical properties are both poorly constrained (Reid et al. 2003; Sokolik and Toon 1999).

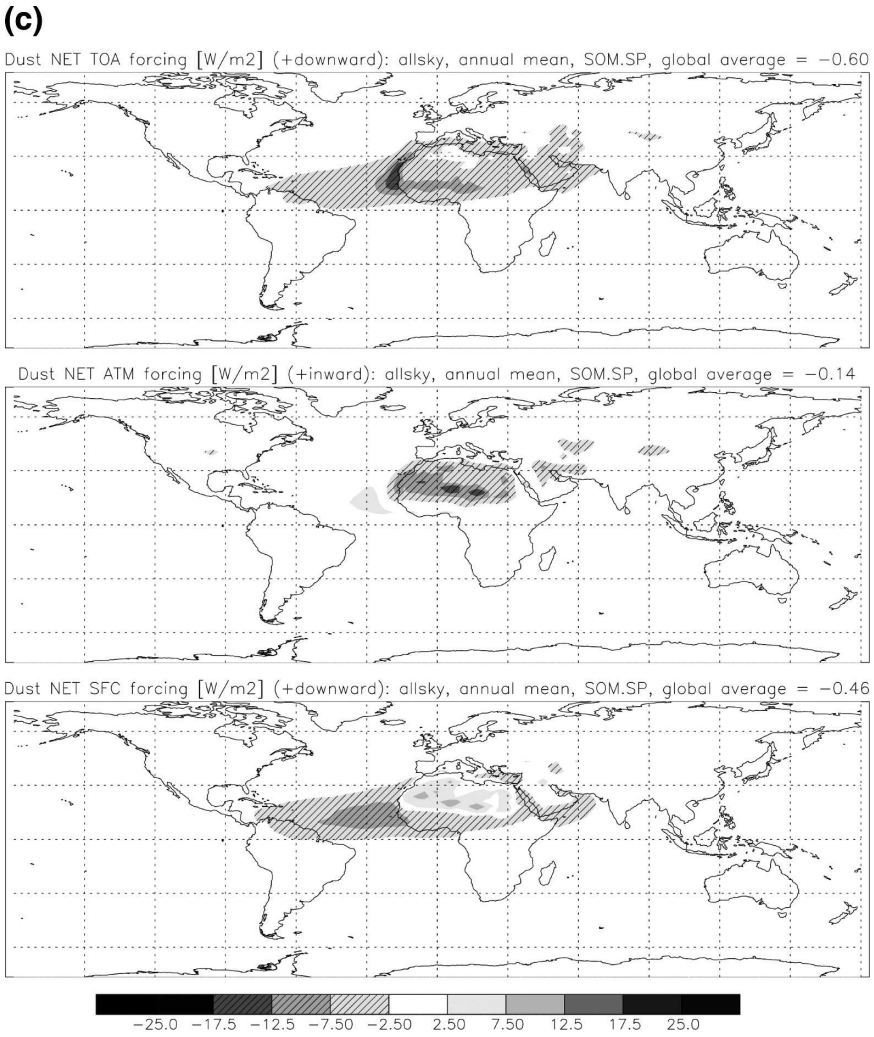

FIG. 2. (*Continued*)

4. Atmospheric responses to dust radiative forcing

a. Precipitation responses

Figure 3 shows JJAS mean precipitations from observed estimates (Xie and Arkin 1997) and the difference between observed estimates and AMIP-simulated precipitation without dust radiative forcing. Only differences statistically significant at a 99% level are shown. Data are averaged for 1979–93, a period in which both observation-based estimates and simulated precipitation are available. The model tends to underestimate precipitation near the ITCZ and distributes precipitation over a broader latitude band leading to overestimates north and south of ITCZ. The exceptions are the western Indian Ocean and Arabian Peninsula, where the model largely overestimates precipitation. Additionally, the model has a double ITCZ-like feature over global oceans. Over West Africa, the model overestimates rainfall to the north of the ITCZ and underestimates over and to the south of the ITCZ. These features are generally in common in all seasons; the latitudinal bands migrate toward north and south with the course of seasons (not shown). Precipitation patterns between AMIP and SOM simulations are similar (not shown), while relatively large differences appear over tropical oceans.

Figure 4 shows precipitation differences due to dust radiative forcings in AMIP (Fig. 4a) and SOM (Fig. 4b) simulations. On global average, dust radiative forcing acts to reduce precipitation: annual precipitation is reduced statistically significantly by 0.83% in SOM (SOM.ND versus SOM.SL) but insignificantly by 0.10% in AMIP (AMIP.ND and AMIP.SL). This reduction is much larger when longwave forcing is neglected (case S) in both AMIP and SOM simulations. The net (shortwave plus longwave) radiative forcing in

TABLE 2. Areal and annual averaged radiative forcing of prognostic dust in the SOM.SP simulation (top four rows) and from other studies (bottom four rows). TOA = top of atmosphere, ATM = within atmosphere, SFC = surface, DOD = dust optical depth at 670 μm (W m^{-2}). Positive downward at TOA and SFC and positive for absorption in ATM.

	SW	LW	Net
Globe; DOD = 0.0381			
TOA	−0.92	+0.31	−0.60
ATM	+0.67	−0.81	−0.14
SFC	−1.59	+1.13	−0.46
North Atlantic Ocean (0°–30°N, 50°–20°W); DOD = 0.198			
TOA	−5.85	+1.06	−4.79
ATM	+3.22	−1.98	+1.25
SFC	−9.07	+3.04	−6.03
North Africa (5°–35°N, 18°W–40°E); DOD = 0.390			
TOA	−8.08	+3.35	−4.73
ATM	+7.38	−11.39	−4.00
SFC	−15.47	+14.74	−0.73
West Indian Ocean (10°S–15°N, 50°–70°E); DOD = 0.040			
TOA	−1.17	+0.26	−0.90
ATM	+0.67	−0.34	+0.34
SFC	−1.84	+0.60	−1.23
Woodward (2001); Globe			
TOA	−0.16	+0.23	+0.07
ATM	+1.06	−0.17	+0.89
SFC	−1.22	+0.40	−0.82
Miller et al. (2004); Globe			
TOA	−0.33	+0.15	−0.18
ATM	+1.49	−0.03	+1.46
SFC	−1.82	+0.18	−1.64
Miller et al. (2006); Globe			
TOA	−0.62	+0.22	−0.40
ATM	+0.67	−0.23	+0.44
SFC	−1.29	+0.45	−0.84
Carlson and Benjamin (1980); Saharan dust over ocean when DOD = 0.2; cloud free			
TOA	–5/–10	+5/+30	0/+20
ATM	+10/+5	+5/–10	+15/–5
SFC	−15/–15	+10/+40	−5/+25

MTP04 is similar to our shortwave forcing due to their small longwave forcing, and their precipitation response is similar to our response in the SOM.S simulation. They show a small increase of precipitation over the western Sahara that we do not obtain. This may be due to the difference in dust optical properties. Our single-scattering albedo is several percent higher than their values (not shown), and their simulation using 10% higher single-scattering albedo does not yield a precipitation increase over the Sahara (see Fig. 16a in MTP04).

The precipitation response to dust radiative forcing is much larger, more consistent, and statistically more significant in SOM than AMIP simulations throughout the globe and especially in the Tropics, although the dust is largely confined to the North Africa and North Atlantic regions (Fig. 1). This is consistent with other studies that have shown that regional forcings in the Tropics have responses through the Tropics and into the extratropics, such as seen with El Niño (e.g., Neelin et al. 2003). Over North Africa, however, the precipitation response is only slightly stronger in SOM simulations. These results imply that precipitation responds indirectly through changes in sea surface temperature, but also directly to dust, especially over North Africa.

The response to dust radiative forcing in SOM simulations (SOM.S–SOM.ND and SOM.SL–SOM.ND) is to reduce precipitation at the peak precipitation over 0°–20°N and enhance precipitation south of this band including the erroneous second ITCZ (15°–5°S), which is pronounced in the Pacific as seen in Fig. 4b and Fig. 5. This pattern can be seen in all seasons and migrates with the course of seasons (not shown). This is the direction toward enhancing the double ITCZ feature, a bias present in all CAM3 simulations. The smaller double ITCZ enhancement in the SOM.SL than in SOM.S means that including longwave forcing improves this bias compared to the case with shortwave forcing alone. The same characteristics can be seen with prescribed shortwave forcing [SOM.SP–SOM.ND; Fig. 4b (bottom)] although the smaller response due to the smaller forcing compared to the case of shortwave forcing of prognostic dust (SOM.S–SOM.ND). This implies that including the longwave radiative forcing of prescribed dust in the base CAM3 should slightly improve the double ITCZ bias.

Previous studies (e.g., Nicholson and Grist 2001; Xue et al. 2004) mention the "dipole" pattern, which refers to the fact that the dry mode in the Sahel tends to accompany greater precipitation along the Guinea Coast. Our simulations show small increase in the Guinea region, which is statistically barely significant in a few spots in the rainy season (JJAS) with SL cases of SOM and AMIP simulations (Figs. 4a,b). However, this does not appear in the annual means since precipitation is decreased in spring and fall in the Sahel (not shown). Such precipitation increase cannot be seen in simulations with cases where longwave forcing is not included (S and SP).

b. Responses in the atmosphere and the surface

Dust radiative forcing has a cooling effect on the surface temperature over most ocean areas of the Northern Hemisphere in SOM simulations, and this effect is strongest in the shortwave only case (S; not shown). Over land, however, including longwave forcing turns cooling into warming over North Africa, the

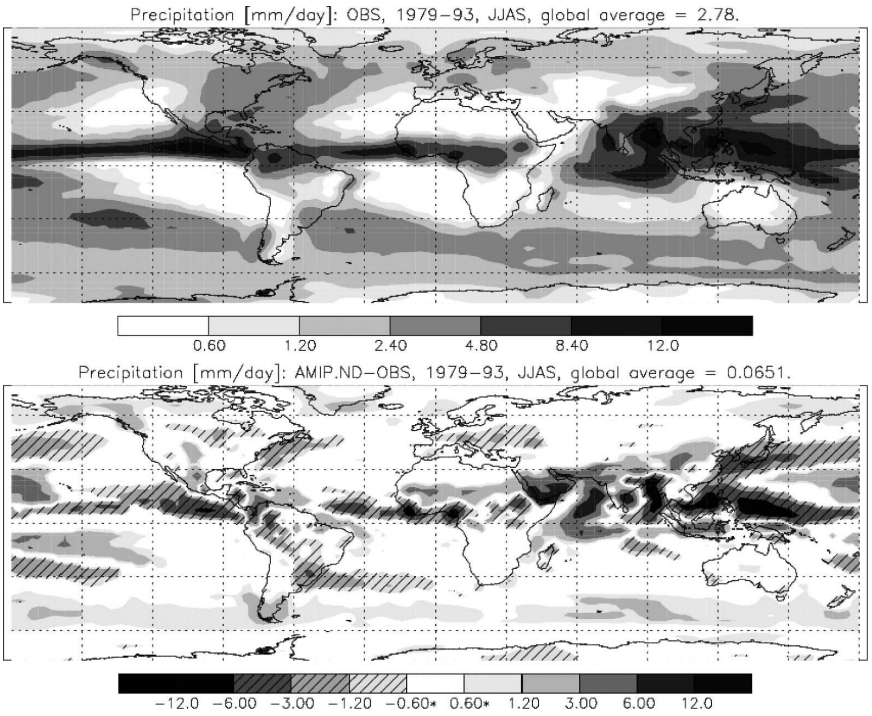

FIG. 3. (top) Observed JJAS precipitation and (bottom) difference between observed and AMIP.ND precipitations (1979–93) (mm day^{-1}). The bottom panel shows statistically significant differences at 99% level only.

Arabian Peninsula, and central Asia (not shown). These are consistent with surface forcing in Fig. 2. Land surface temperature changes in AMIP simulations are similar over North Africa. There is no SST change in AMIP simulations by definition.

In section 4a, it is shown that the sign of the precipitation response over Africa is the same in S and SL cases despite the fact that surface temperature responses over North Africa are opposite as a result of the opposite signs of the forcings at the surface (see bottom panels of Figs. 2a and 2c). Atmospheric forcing of dust is also opposite between S and SL forcings (see middle panels of Figs. 2a and 2c). The fact that these are true not only in SOM but also in AMIP simulations eliminates the possibility of a decisive role of SSTs in precipitation response in North Africa. So let us now look at the responses in atmospheric temperature and circulations for a possible pathway through which the Sahelian rainfall responds to dust radiative forcing.

Figure 6a shows the meridional cross section of the 40-yr European Centre for Medium-Range Weather Forecasts (ECMWF) Re-Analysis (ERA-40; Simmons and Gibson 2000) atmospheric temperature and departure of simulated temperature in the AMIP.ND case. The model has a cool bias over the Sahel in the lower troposphere and warm bias in the upper troposphere of North Africa. The Climate System Model (CSM) simulation reported by Kamga et al. (2005) also shows a negative surface temperature bias over the Sahel compared to the National Centers for Environmental Prediction (NCEP) reanalysis, although it shows larger negative bias over the Sahara (20°–30°N). Figure 6b shows the simulated temperature responses averaged over the longitudes of West Africa in the Sahel rainy season to net (SL) dust radiative forcing in SOM and AMIP simulations. The troposphere cools over and north of the Sahara because of the net radiative forcing in both SOM and AMIP simulations. A stronger cooling occurs when longwave forcing is excluded (not shown). The reason for the tropospheric cooling could be the dust radiative forcing at TOA since it is negative with both S and SL forcings. Therefore, the TOA forcing is considered more important in modulating Sahel precipitation than the surface forcing, in contrast to what is argued in MTP04.

Figure 7a shows the cross section of atmospheric circulation in ECMWF and the AMIP.ND simulation. The simulation shows stronger westerly flow of the West African monsoon (WAM) in the lower troposphere in 10°–25°N and weaker African easterly jet (AEJ) centered at 20°N and 600 hPa than ECMWF. Kamga et al. (2005) have also shown the weaker AEJ in

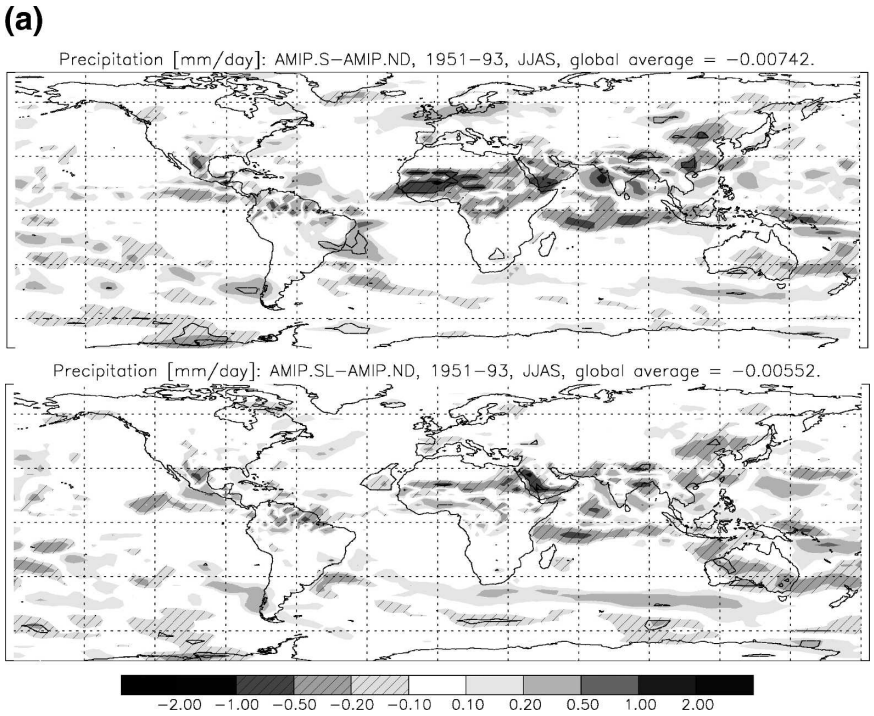

FIG. 4. (a) Differences in AMIP precipitations (1951–93) due to dust radiative forcing (JJAS). [(top) AMIP.S–AMIP.ND and (bottom) AMIP.SL–AMIP.ND. Solid curves show a statistical significance of differences between cases at 99% level.] (b) Same as in (a), but for SOM simulations. [(top) SOM.S–SOM.ND, (middle) SOM.SL–SOM.ND, and (bottom) SOM.SP–SOM.ND.]

the simulation compared to NCEP reanalysis. The simulated response in the atmospheric circulations to the dust radiative forcing in Fig. 7b shows the reduced westerly flow of the WAM, which is consistent with the warming (Fig. 6b) and drying (not shown) near the surface around 20°N since the WAM brings cool and humid oceanic air. As a result, in the lower troposphere the meridional temperature gradient reduces (increases) to the north of 20°N (south of 15°N; see in Fig. 6b). It is also shown that the AEJ is weakened (intensified) to the north (south) of the jet core although this effect is not strong enough to appear as a southward displacement of the AEJ (not shown). Since the AEJ owes its existence to the meridional temperature gradient in the lower troposphere (e.g., Grist and Nicholson 2001), this change in AEJ is consistent with the lower-tropospheric temperature change due to the weakened monsoon and dust radiative cooling. The vertical shear is reduced in 20°–30°N to reduce the possibility for baroclinic instability as a result of reduced monsoon flow and weakened AEJ in this latitude band. The tropical easterly jet (TEJ) located at 0°–20°N and 200 hPa is also weakened in the north of the jet core. All of the weaker WAM, southward displacement (although not clearly visible) of AEJ, smaller vertical shear over the Sahel, and weaker TEJ are features observed in dry years in the Sahel region (Grist and Nicholson 2001).

Although the tropospheric temperature response is much smaller in the AMIP simulations because of the fixed SSTs, the sharper meridional temperature gradients appear to compensate the absolute magnitude of cooling to create the circulation anomalies over North Africa.

5. Impacts of dust on Sahel precipitation relative to those of SSTs, vegetation, and GHGs

Figure 8 shows time series of observed (OBS) and AMIP-simulated precipitation over the Sahel. The April–October precipitation anomaly data are calculated for 10°–20°N and 18°W–20°E from Dai et al. (2004) since the global 2D data (Xie and Arkin 1997) are not available in the wet period (1950s–60s). Simulated precipitation is also averaged for the same region. Ten-year running means have been calculated to eliminate variability on shorter time scales. The uncertainties are estimated using standard errors in the maxi-

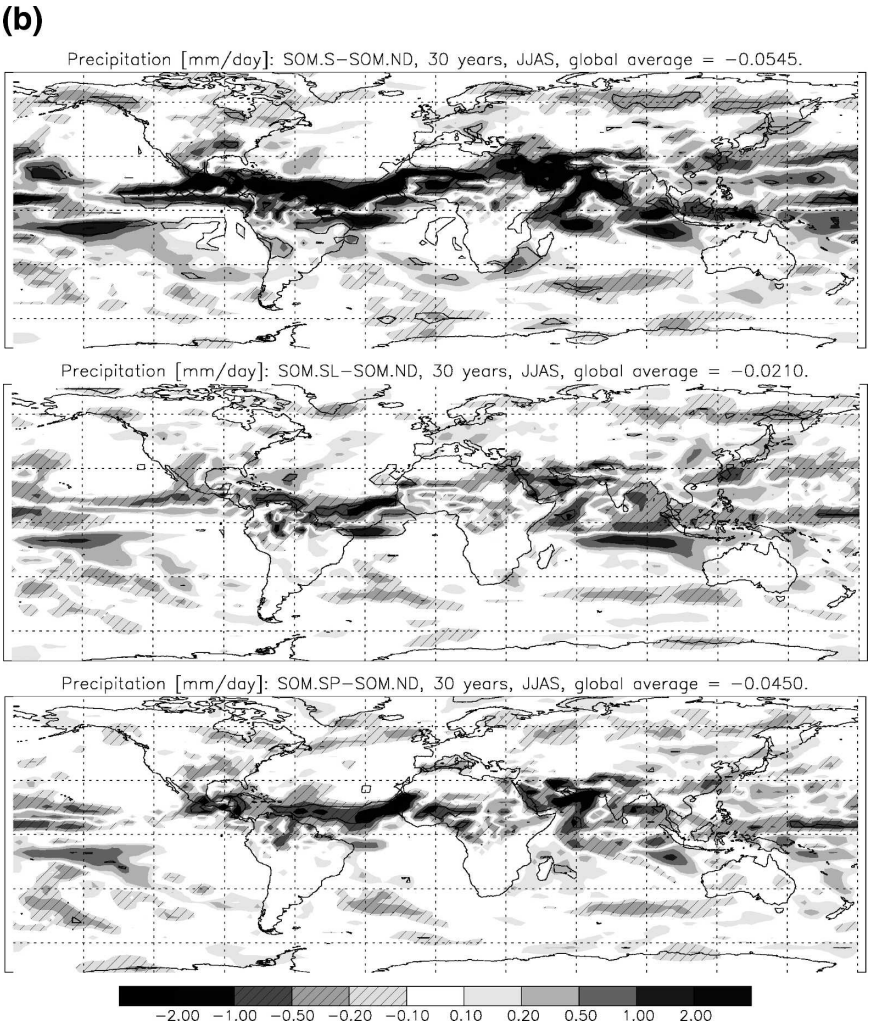

FIG. 4. (*Continued*)

mum and minimum 10-yr periods using the method described in section 2d. The difference in the Sahel precipitation between the driest (1981–90) and the wettest (1951–60) 10-yr periods in the observed record is -0.49 ± 0.11 mm day^{-1}, and this is the change in precipitation we use as a benchmark to evaluate the model results.

In the following sections, we analyze the impacts of changes in SSTs, vegetation, GHGs, and dust radiative forcing on Sahel precipitation by comparing different simulation cases and different periods as summarized in Table 3. Impacts of SSTs are evaluated using wettest and driest 10-yr periods since SSTs vary continuously (not shown), and we are most interested in the maximum magnitude of precipitation change. However, our model only includes fixed vegetation distributions for wet and dry periods and vegetation has by far the largest control on dust emission and loading (Table 3). Therefore, effects of vegetation and dust are evaluated in terms of the differences between wet (1951–70) and dry (1971–93) periods. This makes little changes in the results from the analyses based on wettest and driest 10-yr periods, but the uncertainties decrease due to the larger number of years used.

a. Impacts of the sea surface temperatures

In the AMIP.ND simulation where there is no dust and all forcings other than SSTs are fixed, the difference in precipitation between the driest and wettest 10-yr periods in the model is -0.18 ± 0.13 mm day^{-1} or $36\% \pm 27\%$ of the observed changes (Table 3). Including dust radiative forcing does not change this number when dust loading does not change very much from wet

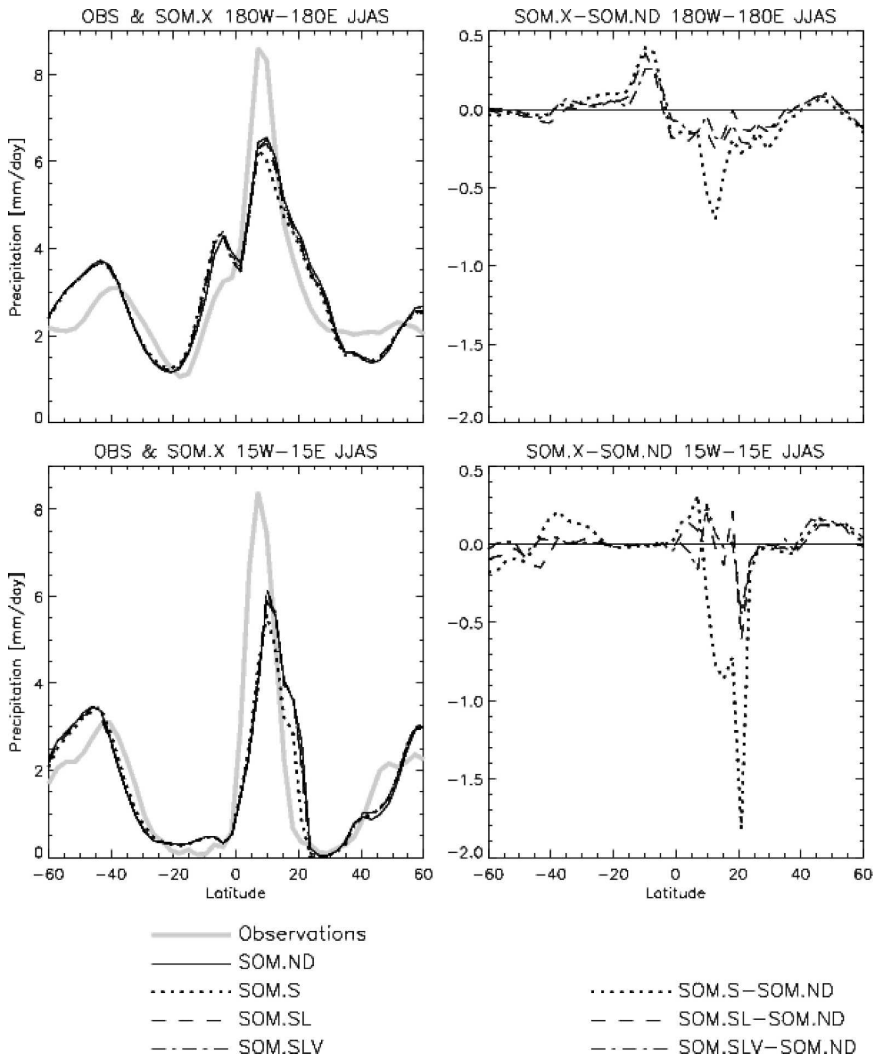

FIG. 5. Zonal mean JJAS (left) observed and SOM simulated precipitations and (right) simulated changes due to dust radiative forcing averaged over (top) all global longitudes and (bottom) 15°W–15°E. Observations are averaged for 1979–2001 and the simulation mean is for all 30 yr.

to dry period (3% increase in AMIP.SL). Using the five ensemble members of the AMIP.F simulations that include radiative forcing by climatologically fixed dust, the maximum precipitation change from wet to dry periods is -0.23 ± 0.05 mm day^{-1} or $+47\% \pm 15\%$ of the observations.

Hoerling et al. (2006) have confirmed the association of interhemispheric SST contrast in the Atlantic basin with the North African monsoon rainfall, which has been identified by previous studies (e.g., Folland et al. 1986; Lamb and Peppler 1992; Rowell et al. 1995). The role of Indian Ocean SST in the Sahel precipitation variability is more controversial. Although Giannini et al. (2003) and Bader and Latif (2003) have identified a strong association between Indian Ocean SST in the Sahel precipitation variability, Hoerling et al. (2006) concluded that Indian Ocean SST is not a leading source of North African precipitation variability in their multimodel approach including models used in Giannini et al. (2003) and Bader and Latif (2003).

In our study, 10-yr running mean Sahel precipitation in observations and AMIP simulations strongly correlates with both the interhemispheric contrast of the Atlantic SSTs ($r = 0.86 \sim 0.89$ in observation as well as AMIP.ND, AMIP.SL, and AMIP.SLV simulations) and West Indian Ocean SST ($r = -0.73 \sim -0.95$). However, since the interhemispheric contrast of the Atlantic SSTs and West Indian Ocean SST are also highly correlated with each other ($r = -0.85$), we cannot separate the effect of one from the other.

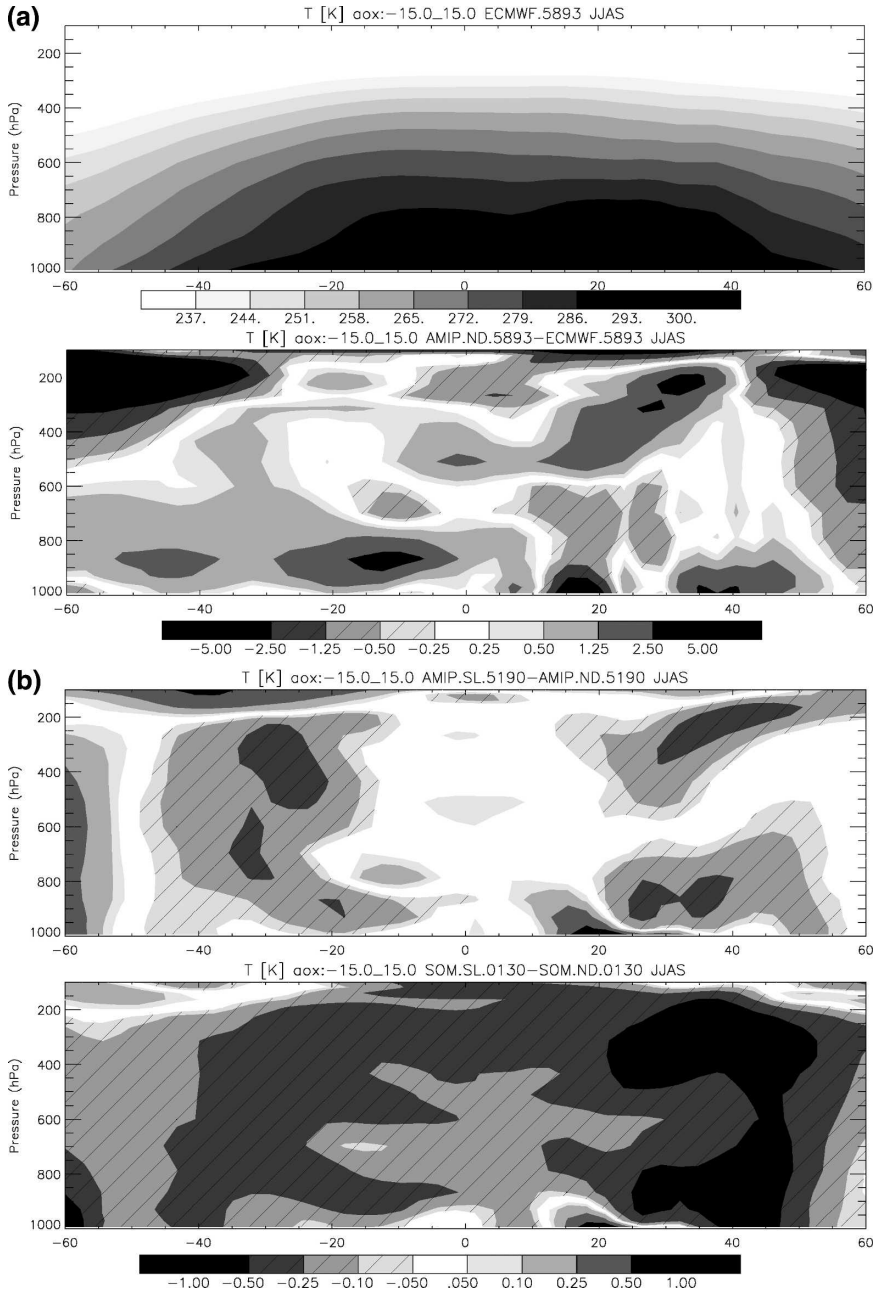

FIG. 6. (a) Meridional cross section of JJAS air temperature in (top) ECMWF and (bottom) AMIP.ND – ECMWF averaged over 15°W–15°E (abscissa is latitudes). (b) Meridional cross section of JJAS air temperature changes due to shortwave and longwave forcing by dust in (top) AMIP (AMIP.SL–AMIP.ND) and (bottom) SOM (SOM.SL–SOM.ND) simulations averaged over 15°W–15°E (abscissa is latitudes).

b. Impacts of Sahel vegetation change

The AMIP.SLV is a simulation using the wet period vegetation for 1951–70 combined with results from the AMIP.SL for 1971–93 using dry period vegetation. Using the wet period vegetation increases the precipitation in this period to make the precipitation trend in the AMIP.SLV more similar to the observations than in the AMIP.SL, but the precipitation decrease is still too small (Fig. 8). The precipitation trend in the AMIP.SLV simulation includes effects of vegetation loss as well as an increase of dust source in the Sahel region. The Sahel precipitation response to the vegetation change between the wet and dry periods is estimated using the

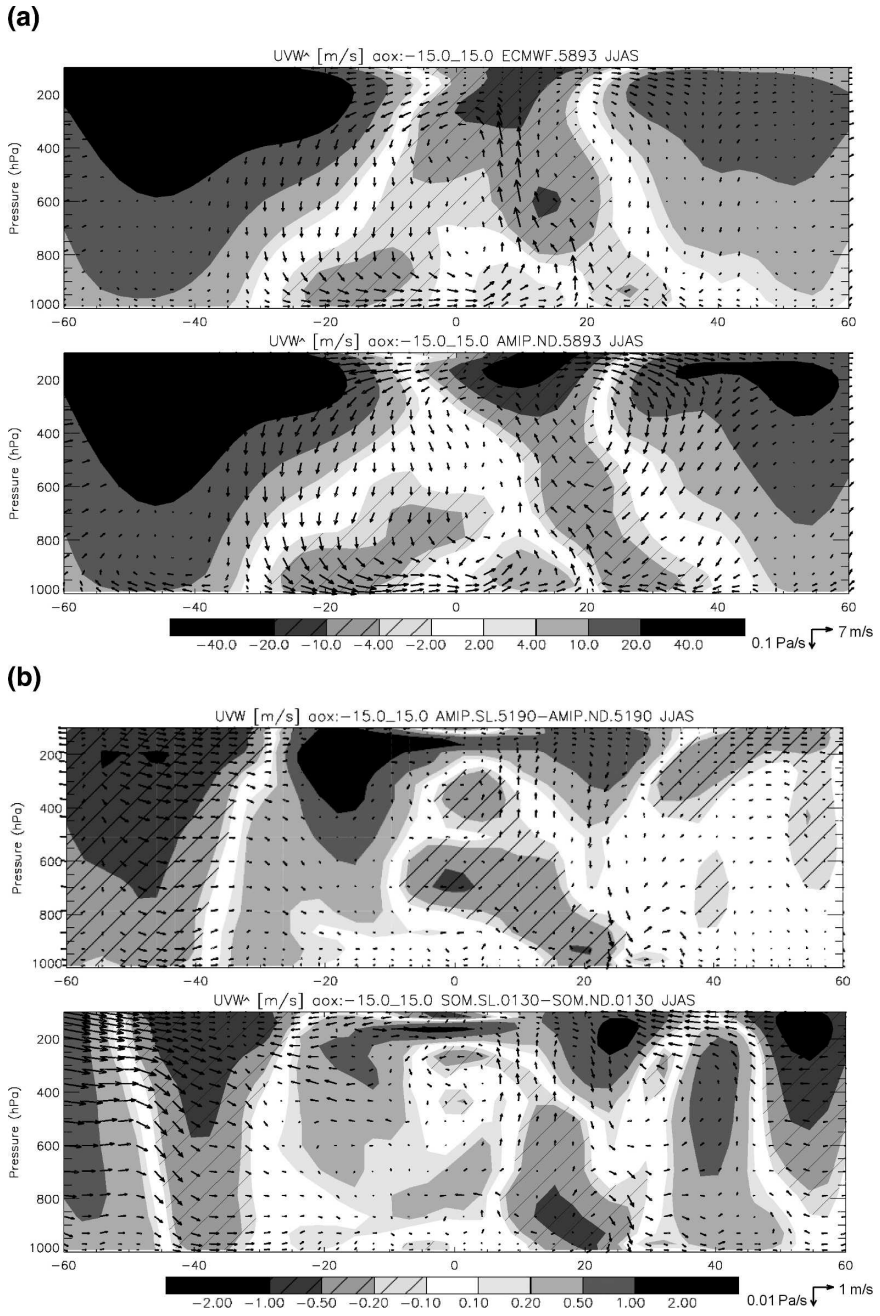

FIG. 7. (a), (b) Same as in Figs. 6a,b, but for atmospheric circulation (shading shows zonal wind component and arrows meridional and vertical components).

difference between the AMIP.ND and AMIP.NDV simulations in the wet period (1951–70). It is obtained to be -0.05 ± 0.07 mm day^{-1} or $10\% \pm 14\%$ of the observed changes in Sahel precipitation, but this is statistically insignificant.

c. *Impacts of greenhouse gas warming*

Another process that might be causing the change in Sahel precipitation is GHG warming. In the equilibrium doubled CO_2 case (SOM.SP2), the model simulates more Sahel precipitation by $+0.13 \pm 0.09$ mm day^{-1} compared to the SOM.SP simulation. This suggests the effect of GHGs of the opposite direction from the observed precipitation change. The GHG impacts in this case contain effects through the sea surfaces, the land surfaces except vegetation change, and the atmosphere. On the other hand, the difference between AMIP.F and AMIP.H in the wet period should give the

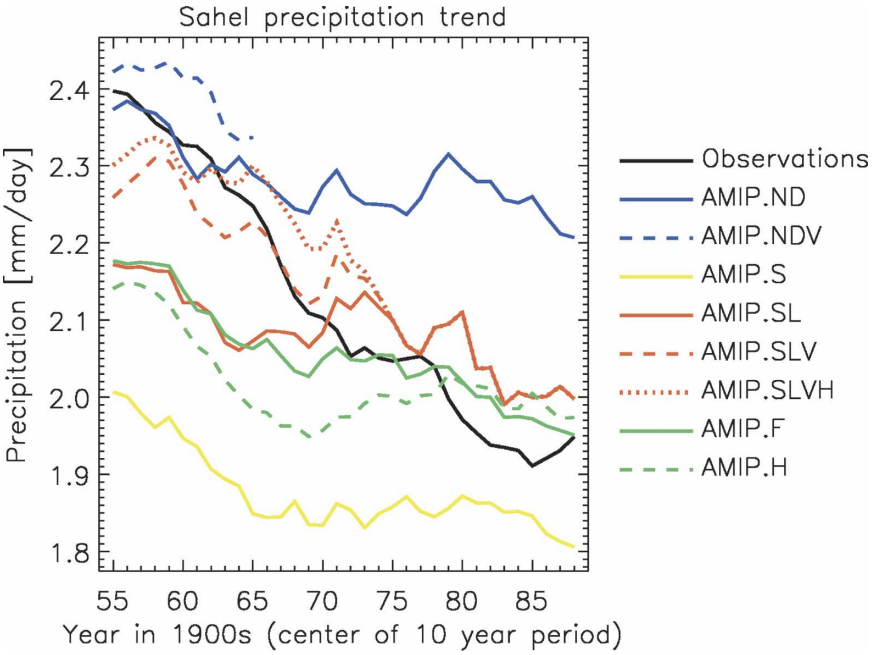

FIG. 8. Annual rainfall trend in the Sahel (10°–20°N, 18°W–20°E) in observations (black), AMIP.ND (blue solid), AMIP.NDV (blue dashed), AMIP.S (yellow), AMIP.SL (red solid), AMIP.SLV (red dashed), AMIP.SLVH (red dotted), AMIP.F (green solid), and AMIP.H (green dashed) simulations. (Precipitation values are 10-yr running means. For example, the abscissa value of 55 represents the period from 1951 to 1960.)

precipitation change due to changes in GHGs and aerosols from the wet to the dry period because in AMIP.F GHGs and aerosols are fixed at the level at 1990 while AMIP.H uses time-varying forcings. In this case the response is through changes of atmosphere and land surface only. The Sahel precipitation response is obtained as $+0.06 \pm 0.03$ mm day^{-1}. In both the SOM and the AMIP simulations, increased GHGs cause increased precipitation in the Sahel, which is opposite to the available observations and consistent with Hoerling et al. (2006).

d. Impacts of dust radiative forcing

The model predicts less Sahel precipitation with dust radiative forcing than without it by -0.20 ± 0.05 mm day^{-1} or 41% ± 16% of observed precipitation change in the Sahel without SST feedback and $-0.22\% \pm 0.06$ mm day^{-1} or 46% ± 16% with SST feedbacks. These are calculated as differences between AMIP.SL and AMIP.ND over the entire period (1951–93) and between SOM.SL and SOM.ND over all 30 yr, respectively. The optical depths of dust at 670 μm averaged over North Africa (8°–35°N, 17°W–30°E) are 0.47 ± 0.01 μm and equal down to the second decimal in both cases. The small difference of the magnitudes of precipitation responses with and without SST feedbacks suggests that the large part of the response in Sahel precipitation from dust radiative forcing is not through SST changes. This is consistent with our hypothesis of importance of the tropospheric cooling over North Africa due to dust TOA radiative forcing in modulating the Sahel precipitation mentioned earlier. The longwave forcing of dust acts to increase the precipitation significantly (AMIP.SL.ALL–AMIP.S.ALL and SOM.SL.ALL–SOM.S.ALL). This means that the longwave forcing considerably offsets the very large effect of shortwave forcing in reducing precipitation.

Including a similar amount of dust in wet and dry periods does not affect the magnitude of the Sahel precipitation change caused by SST changes (AMIP.SL). The AMIP.SLV simulation shows a precipitation decrease of -0.19 ± 0.09 mm day^{-1} or +39% ± 21% of observed precipitation change due to the Sahel vegetation reduction and the resulting increase of dust optical depth by $+0.13 \pm 0.01$ mm day^{-1} or +36% ± 4% relative to the wet period over North Africa. The impact of the increased dust radiative forcing is isolated by subtracting the vegetation impact obtained previously from this value. This results in -0.07 ± 0.09 mm day^{-1} or +15% ± 19% of the observation, and this is statistically insignificant. However, our model likely underestimates the increase of dust between the 1950s and

TABLE 3. Differences of Sahel precipitation in different simulations and periods. D10 (W10): average for driest (wettest) 10-yr period; DP (WP): average for dry (wet) period [1971–93 (1951–70)]; ALL: average for the whole period of simulation: 1951–93 in AMIP, 9 yr for SOM.SP2, and 30 yr for all other SOM simulations. OD: dust optical depth at 670 nm averaged over North Africa; ΔOD: change in dust optical depth.

	Difference (mm day^{-1})	Relative to observed change	Factors and processes involved
OBS.D10–OBS.W10	−0.49 ± 0.11	+100%	Fourfold dust increase, SST, vegetation, and other changes
AMIP.ND.D10–AMIP.ND.W10	−0.18 ± 0.13	+36 ± 27%	SST changes
AMIP.S.D10–AMIP.S.W10	−0.20 ± 0.11	+41 ± 25%	SST changes and small change in dust (ΔOD = +0.03 ± 0.03), SW only
AMIP.SL.D10–AMIP.SL.W10	−0.18 ± 0.14	+37 ± 29%	SST changes and small change in dust (ΔOD = +0.02 ± 0.02)
AMIP.F.D10–AMIP.F.W10	−0.23 ± 0.05	+47 ± 15%	SST changes (fixed dust included)
AMIP.NDV.WP–AMIP.ND.WP	−0.05 ± 0.07	+10 ± 14%	Vegetation change
SOM.SP2.ALL–SOM.SP.ALL	+0.13 ± 0.09	−27 ± 20%	Doubled CO_2
AMIP.F.WP–AMIP.H.WP	+0.06 ± 0.03	−12 ± 7%	Changes in GHGs and other forcings (fixed dust included)
AMIP.SLV.DP–AMIP.SLV.WP	−0.19 ± 0.09	+39 ± 21%	Changes in SSTs, vegetation, and dust (ΔOD = +0.13 ± 0.01 or +36 ± 4%)
AMIP.SLVH.DP–AMIP.SLVH.WP	−0.25 ± 0.09	+51 ± 21%	Changes in SSTs, vegetation, and dust (ΔOD = +0.30 ± 0.01 or +173 ± 6%)
AMIP.SL.ALL–AMIP.ND.ALL	−0.20 ± 0.05	+41 ± 13%	Addition of dust (OD = 0.47 ± 0.01)
SOM.SL.ALL–SOM.ND.ALL	−0.22 ± 0.06	+46 ± 16%	Addition of dust (OD = 0.47 ± 0.01) with SST feedback
AMIP.SL.ALL–AMIP.S.ALL	+0.20 ± 0.06	−42 ± 16%	Addition of dust LW forcing (OD = 0.47 ± 0.01)
SOM.SL.ALL–SOM.S.ALL	+0.39 ± 0.05	−81 ± 21%	Addition of dust LW forcing (OD = 0.47 ± 0.01) with SST feedback
AMIP.SL.WP–AMIP.SLV.WP	−0.12 ± 0.06	+25 ± 13%	Changes in vegetation and dust
(AMIP.SL.WP–AMIP.SLV.WP)–(AMIP.NDV.WP–AMIP.ND.WP)	−0.07 ± 0.09	+15±19%	Change in dust (ΔOD = +0.13 ± 0.01)
AMIP.SL.WP–AMIP.SLVH.WP	−0.18 ± 0.05	+37 ± 13%	Changes in vegetation and dust
(AMIP.SL.WP–AMIP.SLVH.WP)–(AMIP.NDV.WP–AMIP.ND.WP)	−0.13 ± 0.08	+27 ± 18%	Change in dust (ΔOD = +0.30 ± 0.01)
SOM.SL.ALL–SOM.ND.ALL scaled for simulated change of dust optical depth in AMIP.SLV	−0.06 ± 0.02	+12 ± 4%	Change in dust (ΔOD = +0.13 ± 0.01) with SST feedback
SOM.SL.ALL–SOM.ND.ALL scaled for simulated change of dust optical depth in AMIP.SLVH	−0.14 ± 0.04	+29 ± 10%	Change in dust (ΔOD = +0.30 ± 0.01) with SST feedback

1980s by a large degree. The increase of surface dust concentration in the tropical West Atlantic (10°–20°N, 60°–50°W) is estimated as 34% ± 10% in this simulation (not shown), which is much smaller than the reported fourfold increase from late 1960s to 1980s over Barbados (13°N, 60°W; Prospero and Nees 1986; Prospero et al. 1996). This underestimate could be due to many factors, including changes in sources from changes in vegetation or land use (e.g., similar to Mahowald et al. 2002) or other problems in the model. In the AMIP.SLVH simulation, dust emission from North Africa is reduced by a half in the wet period and the resulting increase of dust optical depth from wet to dry period over North Africa is by close to threefold (173% increase between wet and dry periods and 183% increase between least and most dusty 10-yr periods). In this case, the impact of the increased dust radiative forcing is obtained as −0.13 ± 0.08 mm day^{-1} or +27% ± 18% of observed precipitation reduction in the Sahel and this is statistically significant. The precipitation responses to unit optical depth of dust are −0.45 ± 0.15, −0.57 ± 0.71, −0.43 ± 0.28 mm day^{-1}(optical depth)$^{-1}$ in AMIP.SL–AMIP.ND, AMIP.SLV(dry period)–AMIP.SLV(wet period), and AMIP.SLVH(dry period)–AMIP.SLVH(wet period), respectively, and so linearity between impacts and responses roughly holds. As seen above, the SST feedback adds the Sahel precipitation response to dust by a small degree. The values are estimated by scaling the difference of precipitations between the AMIP.SL and AMIP.ND simulations with the ratios of optical depths of dust averaged over North Africa. The obtained estimates are −0.06 ± 0.02 mm day^{-1} or +12% ± 4% or an estimated 34% increase of optical depth and −0.14 ± 0.04 mm day^{-1} or +29% ± 10% for the near-threefold increase.

In summary, our model results suggest that up to 50% of the observed precipitation change can be due to sea surface temperature changes, ~10% from vegetation changes, and up to 30% due to dust radiative forcing and feedbacks. Other factors may include the radiative forcing by changed aerosol loading from biomass burning due to the regional climate change and increased population pressure, which is not considered in this study. This may act through affecting the atmosphere itself and/or the land and sea surface temperatures.

6. Conclusions

This study investigates the role of dust radiative forcing in the Sahelian drought observed in the last three decades of twentieth century using simulations with an atmospheric general circulation model (GCM). Our model shows smaller shortwave and larger longwave forcing of dust than other studies. This is mainly due to the differences in the refractive index and the particle size distribution of dust; compared to many existing studies, we use less absorbing dust and more large particles and fewer small particles than previous modeling studies (e.g., Woodward 2001; Miller et al. 2004) following suggestions from recent observations (Grini and Zender 2004; Hand et al. 2004). As a result, we get net surface warming over the Sahara desert, which is opposite in sign to other studies (e.g., Woodward 2001; Miller et al. 2004).

Our model simulations suggest that radiative forcing of dust acts to reduce the global average precipitation. The precipitation response to dust radiative forcing is generally larger and more consistent when the GCM is coupled with the Slab Ocean Model (SOM), where sea surface temperature (SST) varies in response to radiative forcing, than with AMIP simulation, which is forced by observed SST. A large part of the reduced precipitation occurs over the intertropical convergence zone (ITCZ) around the globe. The CAM3 model is known to have the double ITCZ bias. In our modeling study, the predominantly Northern Hemisphere plume of dust makes the ITCZ weaker and the erroneous Southern Hemisphere ITCZ stronger, and hence effectively increases the double ITCZ bias. This bias is stronger when longwave forcing is neglected as in the default version of the CAM3 model. Over North Africa, contrary to other tropical regions, the difference in the precipitation response between SOM and AMIP is small. This is probably because the tropospheric cooling due to dust radiative forcing at the top of the atmosphere plays an important role in reducing the precipitation over North Africa. The responses of the atmospheric circulation over North Africa are weaker West African monsoon flow, southward displacement of African easterly jet, smaller vertical shear over the Sahel, and weaker tropospheric easterly jet, all of which are features observed in dry years in the Sahel region.

The AMIP simulations with or without dust radiative forcing do produce a drying trend in the Sahel, but the magnitude of this trend is smaller than in the observations. The magnitude of Sahel precipitation reduction is better simulated when dust is increased and vegetation is decreased from the wet 1950–60s to dry 1980–90s. Impacts of SSTs, dust radiative forcing, greenhouse gas (GHG) warming, and vegetation change on Sahel precipitation are isolated by comparing simulations under different scenarios. A large part of the precipitation change is attributed to the observed change in the interhemispheric contrast of the Atlantic SSTs, which may account for up to 50% of the observed precipitation reduction in the Sahel. These SST changes do not appear due to the dust radiative forcing and the GHG warming. The simulated 36% increase in optical depth of dust over North Africa may explain about 15% of the observed precipitation reduction in the Sahel. However, measurements of desert dust at Barbados have suggested a fourfold change in concentration between the 1980s and the 1960s. One of the possible reasons for this large underestimate of the increase of dust is that the model does not include the efficient dust source from the areas under vegetation loss or human land use. If dust emissions in the 1950–60s are reduced by half, which is approximately equivalent to a threefold increase of dust loading in the North Africa and North Atlantic regions, the Sahel precipitation response is estimated to be about 30% of the observed precipitation change between the 1950s and 1980s. The contribution of the Sahel vegetation change is estimated to be about 10% of the observed decrease but is statistically insignificant. The GHG warming acts to increase Sahel precipitation and hence does not explain the observed drying. The radiative forcing by changed aerosol loading from biomass burning, which is not considered in this study, may also have an effect on the Sahel precipitation.

These results are sensitive to the models and methodologies that are used. However, the results are important because they show that the direct radiative forcing of dust has played a role in the observed droughts in the Sahel comparable to the roles played by the sea surface temperatures and vegetation, which have been studied extensively. These results also provide a mechanism whereby drought in the Sahel region can cause increased dust, which then feedbacks to cause a further precipitation reduction.

Acknowledgments. We thank Ron Miller for providing his surface albedo data, Gordon Bonan for consultation in creating vegetation data, Tomoko Matsuo for consultation in statistical methods, the CCSM Climate Variability Working Group for conducting some of the simulation runs analyzed in this study, and the National Center for Atmospheric Research Climate Analysis Section for making data used in this study available. This work was supported by NASA-NAG5-9671, NSF-OCE-9981398, DOE (DE-FG02-02ER-63387), NASA-ESS (NGT5-30413), and the UCSB Affiliates. Computer simulations were conducted at the National Center for Atmospheric Research.

REFERENCES

Anderson, T. W., and J. D. Finn, 1996: *The New Statistical Analysis of Data*. Springer-Verlag, 712 pp.

Arimoto, R., and Coauthors, 2006: Characterization of Asian dust during ACE-Asia. *Global Planet. Change,* **52,** 23–56.

Bader, J., and M. Latif, 2003: The impact of decadal-scale Indian Ocean sea surface temperature anomalies on Sahelian rainfall and the North Atlantic Oscillation. *Geophys. Res. Lett.,* **30,** 2169, doi:10.1029/2003GL018426.

Bevington, P. R., 1988: *Data Reduction and Error Analysis for the Physical Sciences*. McGraw-Hill, 336 pp.

Bonan, G. B., S. Levis, L. Kergoat, and K. W. Oleson, 2002: Landscapes as patches of plant functional types: An integrating concept for climate and ecosystem models. *Global Biogeochem. Cycles,* **16,** 1021, doi:10.1029/2000GB001360.

Carlson, T. N., and J. M. Prospero, 1972: The large-scale movement of Saharan air outbreaks over the northern equatorial Atlantic. *J. Appl. Meteor.,* **11,** 283–297.

——, and S. G. Benjamin, 1980: Radiative heating rates for Saharan dust. *J. Atmos. Sci.,* **37,** 193–213.

Clark, D. B., Y. Xue, R. J. Harding, and P. J. Valdes, 2001: Modeling the impact of land surface degradation on the climate of tropical North Africa. *J. Climate,* **14,** 1809–1822.

Coakley, J. A., Jr., and P. Chylek, 1975: The two-stream approximation in radiative transfer: Including the angle of the incident radiation. *J. Atmos. Sci.,* **32,** 409–418.

Collins, W. D., 1998: A global signature of enhanced shortwave absorption by clouds. *J. Geophys. Res.,* **103,** 31 669–31 679.

——, P. J. Rasch, B. E. Eaton, B. Khattatov, J.-F. Lamarque, and C. S. Zender, 2001: Simulating aerosols using a chemical transport model with assimilation of satellite aerosol retrievals: Methodology for INDOEX. *J. Geophys. Res.,* **106,** 7313–7336.

——, J. K. Hackney, and D. P. Edwards, 2002: An updated parameterization for infrared emission and absorption by water vapor in the National Center for Atmospheric Research Community Atmosphere Model. *J. Geophys. Res.,* **107,** 4664, doi:10.1029/2001JD001365.

——, and Coauthors, 2004: Description of the NCAR Community Atmosphere Model (3.0). NCAR Tech. Note NCAR/TN-464+STR, 214 pp.

——, and Coauthors, 2006a: The Community Climate System Model version 3 (CCSM3). *J. Climate,* **19,** 2122–2143.

——, and Coauthors, 2006b: The formulation and atmospheric simulation of the Community Atmosphere Model version 3 (CAM3). *J. Climate,* **19,** 2144–2161.

Dai, A., P. J. Lamb, K. E. Trenberth, M. Hulme, P. D. Jones, and P. Xie, 2004: The recent Sahel drought is real. *Int. J. Climatol.,* **24,** 1323–1331.

Dickinson, R. E., K. W. Oleson, G. B. Bonan, F. Hoffman, P. Thornton, M. Vertenstein, Z.-L. Yang, and X. Zeng, 2006: The Community Land Model and its climate statistics as a component of the Community Climate System Model. *J. Climate,* **19,** 2302–2324.

Dubovik, O., B. N. Holben, T. F. Eck, A. Smirnov, Y. J. Kaufman, M. D. King, D. Tanré, and I. Slutsker, 2002: Variability of absorption and optical properties of key aerosol types observed in worldwide locations. *J. Atmos. Sci.,* **59,** 590–608.

Dufresne, J.-L., C. Gautier, P. Ricchiazzi, and Y. Fouquart, 2002: Longwave scattering effects of mineral aerosols. *J. Atmos. Sci.,* **59,** 1959–1966.

Fecan, F., B. Marticorena, and G. Bergametti, 1999: Parameterization of the increase of the Aeolian erosion threshold wind friction velocity due to soil moisture for arid and semi-arid area. *Ann. Geophys.,* **17,** 149–157.

Folland, C. K., T. N. Palmer, and D. E. Parker, 1986: Sahel rainfall and worldwide sea temperatures, 1901–85. *Nature,* **320,** 602–607.

Gates, W. L., 1992: AMIP: The Atmospheric Model Intercomparison Project. *Bull. Amer. Meteor. Soc.,* **73,** 1962–1970.

Giannini, A., R. Saravanan, and P. Chang, 2003: Oceanic forcing of Sahel rainfall on interannual to interdecadal time scales. *Science,* **302,** 1027–1030.

Gillette, D. A., and R. Passi, 1988: Modeling dust emission caused by wind erosion. *J. Geophys. Res.,* **93,** 14 233–14 242.

Ginoux, P., 2003: Effects of nonsphericity on mineral dust modeling. *J. Geophys. Res.,* **108,** 4052, doi:10.1029/2002JD002516.

——, M. Chin, I. Tegen, J. M. Prospero, B. Holben, O. Dubovik, and S.-J. Lin, 2001: Sources and distributions of dust aerosols simulated with the GOCART model. *J. Geophys. Res.,* **106,** 20 255–20 273.

Grini, A., and C. S. Zender, 2004: Roles of saltation, sandblasting, and wind speed variability on mineral dust aerosol size distribution during the Puerto Rican Dust Experiment (PRIDE). *J. Geophys. Res.,* **109,** D07202, doi:10.1029/2003JD004233.

Grist, J. P., and S. E. Nicholson, 2001: A study of the dynamic factors influencing the rainfall variability in the West African Sahel. *J. Climate,* **14,** 1337–1359.

Hand, J. L., N. M. Mahowald, Y. Chen, R. L. Siefert, C. Luo, A. Subramaniam, and I. Fung, 2004: Estimates of soluble iron from observations and a global mineral aerosol model: Biogeochemical implications. *J. Geophys. Res.,* **109,** D17205, doi:10.1029/2004JD004574.

Haywood, J. M., R. P. Allan, I. Culverwell, T. Slingo, S. Milton, J. Edwards, and N. Clerbaux, 2005: Can desert dust explain the outgoing longwave radiation anomaly over the Sahara during July 2003? *J. Geophys. Res.,* **110,** D05105, doi:10.1029/2004JD005232.

Hoerling, M., J. Hurrell, J. Eischeid, and A. Phillips, 2006: Detection and attribution of 20th century northern and southern African rainfall change. *J. Climate,* **19,** 3989–4008.

Houghton, J. T., Y. Ding, D. J. Griggs, M. Noguer, P. J. van der Linden, X. Dai, K. Maskell, and C. A. Johnson, Eds., 2001: *Climate Change 2001: The Scientific Basis.* Cambridge University Press, 944 pp.

Iversen, J. D., and B. R. White, 1982: Saltation threshold on Earth, Mars and Venus. *Sedimentology,* **29,** 111–119.

Kamga, A. F., G. S. Jenkins, A. T. Gaye, A. Garba, A. Sarr, and A. Adedoyin, 2005: Evaluating the National Center for Atmospheric Research climate system model over West Africa: Present-day and the 21st century A1 scenario. *J. Geophys. Res.,* **110,** D03106, doi:10.1029/2004JD004689.

Karyampudi, V. M., and Coauthors, 1999: Validation of the Saharan Dust Plume Conceptual Model using lidar, Meteosat, and ECMWF data. *Bull. Amer. Meteor. Soc.,* **80,** 1045–1075.

Lamb, P. J., and R. A. Peppler, 1992: Further case studies of tropical Atlantic surface atmospheric and oceanic patterns associated with sub-Saharan drought. *J. Climate,* **5,** 476–488.

Li, F., A. M. Vogelmann, and V. Ramanathan, 2004: Saharan dust aerosol radiative forcing measured from space. *J. Climate,* **17,** 2558–2571.

Luo, C., N. M. Mahowald, and J. del Corral, 2003: Sensitivity study of meteorological parameters on mineral aerosol mobilization, transport, and distribution. *J. Geophys. Res.,* **108,** 4447, doi:10.1029/2003JD003483.

Mahowald, N. M., and C. Luo, 2003: A less dusty future? *Geophys. Res. Lett.,* **30,** 1903, doi:10.1029/2003GL017880.

——, C. S. Zender, C. Luo, D. Savoie, O. Torres, and J. del Corral, 2002: Understanding the 30-year Barbados desert dust record. *J. Geophys. Res.,* **107,** 4561, doi:10.1029/2002JD002097.

——, C. Luo, J. del Corral, and C. S. Zender, 2003: Interannual variability in atmospheric mineral aerosols from a 22-year model simulation and observational data. *J. Geophys. Res.,* **108,** 4352, doi:10.1029/2002JD002821.

——, D. Muhs, S. Levis, M. Yoshioka, C. S. Zender, and P. J. Rasch, 2006: Change in atmospheric mineral aerosols in response to climate: Last glacial period, pre-industrial, modern, and doubled carbon dioxide climates. *J. Geophys. Res.,* **111,** D10202, doi:10.1029/2005JD006653.

Marticorena, B., and G. Bergametti, 1995: Modeling the atmospheric dust cycle: 1. Design of a soil-derived dust emission scheme. *J. Geophys. Res.,* **100,** 16 415–16 430.

Miller, R. L., and I. Tegen, 1998: Climate response to soil dust aerosols. *J. Climate,* **11,** 3247–3267.

——, I. Tegen, and J. Perlwitz, 2004: Surface radiative forcing by soil dust aerosols and the hydrologic cycle. *J. Geophys. Res.,* **109,** D04203, doi:10.1029/2003JD004085.

——, and Coauthors, 2006: Mineral dust aerosols in the NASA Goddard Institute for Space Sciences ModelE atmospheric general circulation model. *J. Geophys. Res.,* **111,** D06208, doi:10.1029/2005JD005796.

Neelin, J. D., C. Chou, and H. Su, 2003: Tropical drought regions in global warming and El Niño teleconnections. *Geophys. Res. Lett.,* **30,** 2275, doi:10.1029/2003GL018625.

Nicholson, S. E., 1995: Variability of African rainfall on interannual and decadal time scales. *Natural Climate Variability on Decade-to-Century Time Scales,* National Research Council, National Academy Press, 32–43.

——, 2000: Land surface processes and Sahel climate. *Rev. Geophys.,* **38,** 117–139.

——, and J. P. Grist, 2001: A conceptual model for understanding rainfall variability in the West African Sahel on interannual and interdecadal timescales. *Int. J. Climatol.,* **21,** 1733–1757.

Patterson, E. M., 1981: Optical properties of the crustal aerosol: Relation to chemical and physical characteristics. *J. Geophys. Res.,* **86,** 3236–3246.

Prospero, J. M., and R. T. Nees, 1986: Impact of the North African drought and El Niño on mineral dust in the Barbados trade winds. *Nature,* **320,** 735–738.

——, and P. J. Lamb, 2003: African droughts and dust transport to the Caribbean: Climate change implications. *Science,* **302,** 1024–1027.

——, and Coauthors, 1996: Atmospheric deposition of nutrients to the North Atlantic Basin. *Biogeochemistry,* **35,** 27–73.

Ramanathan, V., and P. Downey, 1986: A nonisothermal emissivity and absorptivity formulation for water vapor. *J. Geophys. Res.,* **91,** 8649–8666.

Ramankutty, N., and J. A. Foley, 1999: Estimating historical changes in global land cover: Croplands from 1700 to 1992. *Global Biogeochem. Cycles,* **13,** 997–1027.

Rasch, P. J., W. D. Collins, and B. E. Eaton, 2001: Understanding the Indian Ocean Experiment (INDOEX) aerosol distributions with an aerosol assimilation. *J. Geophys. Res.,* **106,** 7337–7356.

Reid, J. S., and Coauthors, 2003: Comparison of size and morphological measurements of coarse mode dust particles from Africa. *J. Geophys. Res.,* **108,** 8593, doi:10.1029/2002JD002485.

Rowell, D. P., C. K. Folland, K. Maskell, and M. N. Ward, 1995: Variability of summer rainfall over tropical North Africa (1906–1992): Observations and modelling. *Quart. J. Roy. Meteor. Soc.,* **121,** 669–704.

Simmons, A. J., and J. K. Gibson, 2000: The ERA-40 Project Plan. ECMWF ERA-40 Project Rep. Series No. 1, 63 pp. [Available online at http://www.ecmwf.int/publications/.]

Sinyuk, A., O. Torres, and O. Dubovik, 2003: Combined use of satellite and surface observations to infer the imaginary part of refractive index of Saharan dust. *Geophys. Res. Lett.,* **30,** 1081, doi:10.1029/2002GL016189.

Sokolik, I. N., and O. B. Toon, 1999: Incorporation of mineralogical composition into models of the radiative properties of mineral aerosol from UV to IR wavelengths. *J. Geophys. Res.,* **104** (D8), 9423–9444.

——, A. Andronova, and T. C. Johnson, 1993: Complex refractive index of atmospheric dust aerosols. *Atmos. Environ.,* **27A,** 2495–2502.

Stephenne, N., and E. F. Lambin, 2001: A dynamic simulation model of land-use changes in Sudano-Sahelian countries of Africa (SALU). *Agric. Ecosyst. Environ.,* **85,** 145–161.

Taylor, C. M., E. F. Lambin, N. Stephenne, R. J. Harding, and R. L. H. Essery, 2002: The influence of land use change on climate in the Sahel. *J. Climate,* **15,** 3615–3629.

Taylor, J. R., 1982: *An Introduction to Error Analysis: The Study of Uncertainties in Physical Measurements*. University Science Books, 270 pp.

Tegen, I., and I. Fung, 1994: Modeling of mineral dust in the atmosphere: Sources, transport, and optical thickness. *J. Geophys. Res.,* **99,** 22 897–22 914.

——, and ——, 1995: Contribution to the atmospheric mineral aerosol load from land surface modification. *J. Geophys. Res.,* **100,** 18 707–18 726.

Tucker, C. J., and S. E. Nicholson, 1999: Variations in the size of the Sahara, 1980 to 1997. *Ambio,* **28,** 587–591.

Volz, F. E., 1973: Infrared optical constants of ammonium sulfate, Sahara dust, volcanic pumice, and flyash. *Appl. Opt.,* **12,** 564–568.

Wang, G., E. A. B. Eltahir, J. A. Foley, D. Pollard, and S. Levis, 2004: Decadal variability of rainfall in the Sahel: Results from the coupled GENESIS-IBIS atmosphere-biosphere model. *Climate Dyn.,* **22,** 625–637.

White, B. R., 1979: Soil transport by winds on Mars. *J. Geophys. Res.,* **84,** 4643–4651.

Woodward, S., 2001: Modeling the atmospheric life cycle and radiative impact of mineral dust in the Hadley Centre climate model. *J. Geophys. Res.,* **106,** 18 155–18 166.

Xie, P., and P. A. Arkin, 1997: Global precipitation: A 17-year monthly analysis based on gauge observations, satellite estimates, and numerical model outputs. *Bull. Amer. Meteor. Soc.,* **78,** 2539–2558.

Xue, Y., 1997: Biosphere feedback on regional climate in tropical North Africa. *Quart. J. Roy. Meteor. Soc.,* **123,** 1483–1515.

——, and J. Shukla, 1993: The influence of land surface properties on Sahel climate. Part I: Desertification. *J. Climate,* **6,** 2232–2245.

——, and ——, 1998: Model simulation of the influence of global SST anomalies on Sahel rainfall. *Mon. Wea. Rev.,* **126,** 2782–2792.

——, H.-M. H. Juang, W.-P. Li, S. Prince, R. DeFries, Y. Jiao, and R. Vasic, 2004: Role of land surface processes in monsoon development: East Asia and West Africa. *J. Geophys. Res.,* **109,** D03105, doi:10.1029/2003JD003556.

Zender, C. S., B. Huisheng, and D. Newman, 2003a: Mineral dust entrainment and deposition (DEAD) model: Description and 1990s dust climatology. *J. Geophys. Res.,* **108,** 4416, doi:10.1029/2002JD002775.

——, D. Newman, and O. Torres, 2003b: Spatial heterogeneity in aeolian erodibility: Uniform, topographic, geomorphic, and hydrologic hypotheses. *J. Geophys. Res.,* **108,** 4543, doi:10.1029/2002JD003039.

Zeng, N., J. D. Neelin, K.-M. Lau, and C. J. Tucker, 1999: Enhancement of interdecadal climate variability in the Sahel by vegetation interaction. *Science,* **286,** 1537–1540.

Zhang, J., and S. A. Christopher, 2003: Longwave radiative forcing of Saharan dust aerosols estimated from MODIS, MISR, and CERES observations on Terra. *Geophys. Res. Lett.,* **30,** 2188, doi:10.1029/2003GL018479.